7-10-2024

Synoptic Drivers of Extreme Precipitation in the Upper Yuba Watershed of California

Emma Nichole Russell
Portland State University

Synoptic Drivers of Extreme Precipitation in the Upper Yuba Watershed of California

by

Emma Nichole Russell

A thesis submitted in partial fulfillment of the
requirements for the degree of

Master of Science
in
Geography

Thesis Committee:
Paul C. Loikith, Chair
Laís G. Fernandes
Andrew C. Martin
Emily A. Slinskey

Portland State University
2024

Abstract

The United States state of California is vulnerable to both droughts and extreme precipitation events due to the timing and processes of precipitation in the region. California's annual precipitation is dependent on a few strong storms and in addition to its Mediterranean climate, leads to great variability in precipitation both within and across years. While efforts to reduce the impacts of extreme precipitation events have been implemented, forecasting for these events remains a challenge in regions with complex terrain and dynamic meteorological drivers. In order to improve forecasting and preparedness for such events, it is important to understand the range of atmospheric drivers that lead to extreme precipitation, particularly on a small scale. Here we aim to better understand the variety of meteorological mechanisms resulting in wet season (October–March) extreme precipitation in the Upper Yuba watershed of California from 1980 to 2021. We implement an Extended self-organizing maps (SOM) approach to cluster and evaluate integrated water vapor transport (IVT) patterns during and preceding extreme precipitation days as 12 distinct 5-day patterns. Patterns show a range of storm types, largely characterized by southerly to southwesterly moisture transport driven by anomalously low sea level pressure and 300 hPa geopotential heights. Pattern orientation and intensities vary, with greater IVT magnitudes generally associated with higher watershed precipitation. Some patterns also show relatively low moisture transport, indicating the presence of additional drivers of regional precipitation. The methodology and evaluation of this study can aid in improving hydrometeorological forecasting in the Upper Yuba and other societally important watersheds.

Acknowledgments

I first want to thank my advisor, Dr. Paul Loikith, for being an incredible mentor during both my undergraduate and graduate programs. Thank you for believing in me and for the amazing opportunities you have provided me with. I am incredibly grateful for the enduring encouragement and reassurance during my moments of fear and doubt and for your kindness, thoughtfulness, and patience with me during this journey.

I also want to acknowledge the members of the Portland State Climate Science Lab for their support, companionship, and friendships. Thank you to my family and community for their constant encouragement and for being there to celebrate the accomplishments together. I feel so grateful to have been surrounded by such kind and generous people during this process. Lastly, a great thanks to all of my committee members, Drs. Laís Fernandes, Andrew Martin, and Emily Slinskey for providing invaluable guidance and feedback on this project.

Support for this research was provided by a subaward from the University of California San Diego Forecast-Informed Reservoir Operations project.

Table of Contents

List of Figures

1. Introduction

1.1. Background and Motivation

Extreme precipitation has profound impacts on food and water security, human health, and infrastructure across the globe. Flooding due to extreme precipitation leads to the loss of lives, property, and infrastructure as well as an increase in water-borne disease, water insecurity, and economic losses (Cordeira et al., 2019; Corringham et al., 2019; Pörtner, H.-O., 2022; Reidmiller et al., 2017; Seneviratne et al., 2021). With rising global temperatures, extreme precipitation events have increased in both frequency and intensity, as a warmer atmosphere has a higher capacity for moisture storage (Seneviratne et al., 2021). This trend is expected to continue with a warming climate, increasing the potential for flooding and related damages in the future (Seneviratne et al., 2021).

The United States (US) state of California is uniquely vulnerable to extreme precipitation due to its Mediterranean climate which consists of pronounced dry summers and wet winters, which results in much of its precipitation occurring over just a few months (Dettinger et al., 2011). Additionally, precipitation in California is primarily driven by large extratropical storms and orographic lift due to its location in the mid-latitude storm track and mountainous topography making it susceptible to intense storms, particularly when subtropical moisture is available for transport to the state (Dettinger, 2013; Dettinger et al., 2011; Ralph et al., 2005; Smith et al., 2010). Annual precipitation amounts are largely regulated by the occurrence of these strong storms, leading to great precipitation variability both within years and from year to year (Dettinger et al., 2011)**.** The influence of and susceptibility to these large storms in California pose a threat to the

populated region that has historically experienced wintertime flooding, landslides, and erosion (Barth et al., 2015; Cordeira et al., 2019; Corringham et al., 2019; Dettinger, 2013; Neiman et al., 2008; Ralph et al., 2006). On the contrary, intense storms can also provide well-needed precipitation to California during periods of dryness as they reduce precipitation deficits, eliminate droughts, and increase water supply (Dettinger, 2013; Dettinger et al., 2011).

To best mitigate the impacts of extreme precipitation and improve hydrometeorological forecasting in a state prone to both drought and floods, several studies have investigated the meteorological processes and features driving these events. Along the US West Coast, precipitation is generally associated with North Pacific extratropical cyclones and a prefrontal low-level jet (LLJ) ahead of a cold front (Ralph et al., 2005). These LLJs exist alongside narrow corridors of enhanced water vapor transport known as atmospheric rivers (ARs), which are largely responsible for the horizontal transport of moisture into the midlatitudes (Barlow et al., 2019; Ralph et al., 2004; Zhu & Newell, 1998). Much of California's extreme precipitation and flooding events are associated with these ARs; the resulting precipitation is enhanced by the orographic lifting of the moisture-rich air over coastal and interior mountain ranges, which are often aligned perpendicular to the landfalling ARs (Dettinger et al., 2011; Ralph et al., 2006; Smith et al., 2010).

Certain characteristics of ARs lead to greater precipitation and regional impacts across the state of California. ARs tend to be stronger, more frequent, and more impactful in the winter season, resulting in higher rises in soil moisture, increased river streamflow,

and more intense flooding (Lamjiri et al., 2017; Neiman et al., 2008; Ralph et al., 2012; Slinskey et al., 2020). Those with a south-to-southwesterly orientation tend to produce the highest precipitation in the coastal Russian River and Santa Ana River watersheds (Cannon et al., 2018; Hecht & Cordeira, 2017; Ralph et al., 2012). Additionally, an evaluation of the Yuba and Feather watersheds found that precipitation is largely driven by storm and wind field orientation, with maximum precipitation occurring with a 217° and 240° (southwesterly) wind field in the Yuba and Feather watersheds, respectively (Ohara et al., 2017).

ARs and extreme precipitation in California are driven by preferred atmospheric circulation patterns and meteorological processes that describe the dynamic drivers of these events. Landfalling ARs tend to be associated with a North Pacific surface pressure dipole consisting of low pressure in the northeast Pacific and high pressure offshore of Southern California, a pattern that enhances moisture transport from the tropics (Cannon et al., 2018; Guirguis et al., 2018; Harris & Carvalho, 2018). Repetitive omega blocks and persistent negatively tilted troughs over the Gulf of Alaska were present in the 2016–2017 winter season, a particularly intense season that experienced a large number of extreme precipitation events (Moore et al., 2020). Rossby wave breaking (RWB) events also contribute to extreme precipitation by driving the intrusion of low potential vorticity (PV) air towards the tropics, enhancing baroclinic development and promoting cyclogenesis (Moore et al., 2020; Ryoo et al., 2013). In addition, California's extreme precipitation is amplified by certain modes of climate variability, including the positive

phase of the El Niño-Southern Oscillation (ENSO) and Pacific Decadal Oscillation (PDO) (Dettinger et al., 2011; Fernandes & Loikith, 2023).

1.2. Objectives

California's pronounced wet and dry seasons pose a challenge for water management in the state as reservoirs fed by rain and snowmelt are utilized to enhance water storage for the dry season while simultaneously mitigating flood risks in the wet season. One critical component to improving reservoir operations in California and reducing the risk of hazards is to improve the understanding of extreme precipitation drivers in the region, specifically at the watershed scale. Although the synoptic patterns associated with extreme precipitation in California are broadly understood, there remains uncertainty as to the drivers of more localized extreme precipitation, especially in regions of complex and meteorologically influential terrain where subtle differences in atmospheric patterns can modulate local precipitation amounts and intensity.

To enhance our understanding of watershed-scale extreme precipitation, this study aims to evaluate the drivers of extreme precipitation in California's Upper Yuba watershed (Fig. 1). This evaluation identifies and describes the key synoptic patterns and processes associated with wet season (October–March) extreme precipitation in the Upper Yuba using climate reanalysis data and the self-organizing maps (SOM) clustering approach. The results of this analysis will not only aid in better understanding the key meteorological drivers of extreme precipitation in the Upper Yuba watershed but also provide a basis for improved interpretation of hydrometeorological forecasting in this and other societally important watersheds.

1.3. Region

The Upper Yuba watershed is located in the foothills of the Sierra Nevada mountain range making it topographically complex and a challenging area for precipitation forecasting. This region has experienced historical flooding that has impacted the nearby population of the Central Valley (Fridirici & Shelton, 2000). In addition, the watershed contains the New Bullards Bar Dam, a reservoir managed by the US Army Corp of Engineers (USACE) to store water and manage flood risks, with its management benefitting from an improved understanding of precipitation over the region.

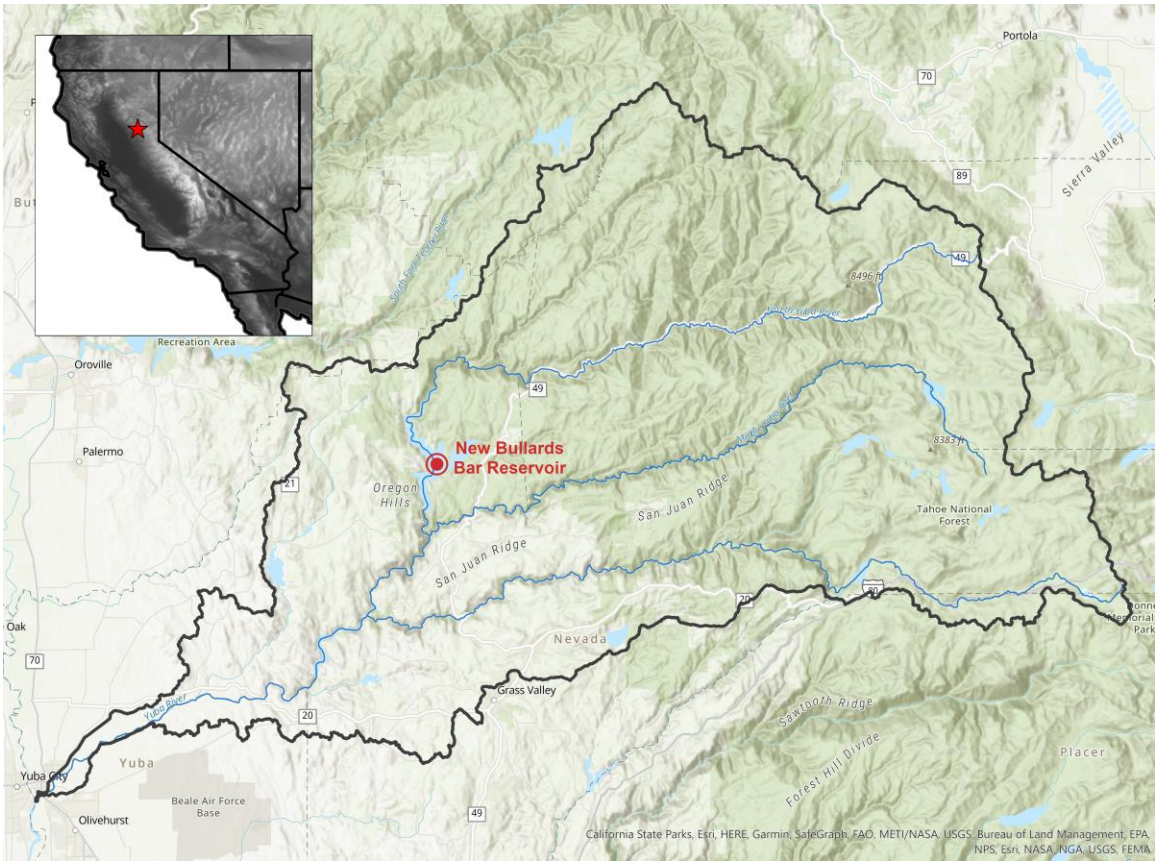

Figure 1. The Upper Yuba watershed and its main reservoir, the New Bullards Bar Reservoir (marked by a red circle), and its location within California (marked with a red star) in the upper left topographic map.

2. Data

Daily accumulated precipitation data are from the Gridded Surface Meteorological (gridMET; Abatzoglou, 2013) Dataset, a high-resolution (1/24°, ~4 km, grid) dataset of daily surface meteorological variables developed using the spatial attributes of Parameter Regression on Independent Slopes Method (PRISM; Daly et al., 1994) data and temporal attributes of North American Land Data Assimilation System, Phase 2 (NLDAS-2; Xia et al., 2012a; Xia et al., 2012b). 300 hPa geopotential height (Z300), sea level pressure (SLP), 850 hPa temperature, 300 and 850 hPa wind speeds, and integrated water vapor transport (IVT) are from Modern-Era Retrospective Analysis for Research and Applications, Version 2 (MERRA-2), provided on a 0.5° latitude by 0.625° longitude grid (Gelaro et al., 2017). The Guan and Waliser Global Atmospheric River Database, MERRA-2 Version 3 (Guan et al., 2018; Guan & Waliser, 2015, 2019), was used as a catalog of AR occurrences over the climatological period, with the same gridded characteristics as MERRA-2.

3. Methodology

3.1. Extreme Precipitation Days

Extreme precipitation days were defined as those exceeding the 90th percentile of daily mean watershed precipitation in the wet season (October–March) gridMET record from 1980 to 2021. The wet season, as defined here, accounts for nearly 70% of annual watershed precipitation and incorporates California's rainy season as well as the onset of atmospheric river activity (Harris & Carvalho, 2018; Kim et al., 2013; Luković et al., 2021; Slinskey et al., 2020). Days with mean watershed precipitation of less than 2 millimeters were excluded from the distribution prior to computing the 90th percentile threshold. In total, 260 extreme precipitation days were identified and evaluated for the study (Fig. 2).

3.2. Climatologies and AR Presence

Daily mean MERRA-2 data were computed from the available 1-hourly (IVT) and 3-hourly (all other variables) resolutions. Daily standardized anomalies for Z300, SLP, and 850 hPa temperature were computed using the wet season climatological means and standard deviations. Daily precipitation anomalies were computed as a fraction of the climatological wet season mean. The presence of ARs on extreme precipitation days was defined as any occurrence throughout the day over any portion of the watershed, bounded by 38.5° and 40.5° north latitude and -122.5° and -120.0° west longitude, from the 6-hourly AR catalog data.

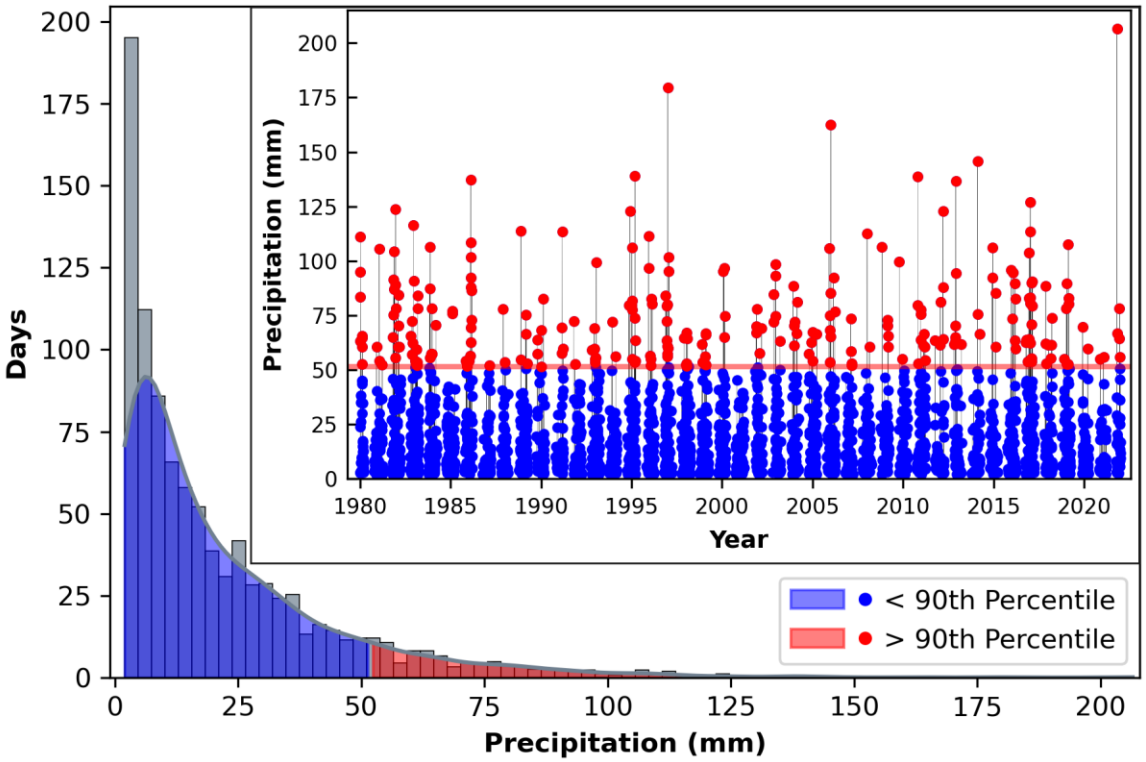

Figure 2. Upper Yuba watershed wet season precipitation climatology (from 1980 to 2021) as daily mean precipitation values (in millimeters, inside) and the precipitation frequency distribution with a kernel density estimation curve (outside). Days below the climatological 90th percentile are in blue, while those exceeding the extreme threshold are marked in red.

3.3. Self-Organizing Maps

The self-organizing map (SOM) technique, initially developed by Kohonen (1982), has been used widely to study synoptic climatology, large-scale circulation patterns, and extreme weather events (Aragon et al., 2020; Gibson et al., 2017; Hewitson & Crane, 2002; Liu et al., 2011; Loikith et al., 2017; Schlef et al., 2019; Sheridan & Lee, 2011). The SOM is a form of unsupervised neural network that assists in clustering patterns from large datasets into an $m \times n$ matrix of groups known as 'nodes' to evaluate the pattern composition within a dataset. The adjustable SOM matrix size allows for the optimization of the output's applicability and interpretability. A larger SOM matrix

captures more pattern variability within the data but is often at the expense of increased pattern redundancy between nodes and diminished interpretability. On the other hand, a smaller SOM provides less information about pattern variability but can enhance interpretability by reducing node redundancy. Finding an appropriate SOM size can improve the effectiveness of such a methodology.

SOMs first require an initialization of linear or randomized input data to be seeded into each node. Next, an iterative process where each input vector is assigned to the node with the shortest Euclidean distance between it and the node data is performed. When each vector is assigned to a node, that node pattern is nudged closer to the input data while the surrounding nodes (according to the user-defined neighborhood radius) are nudged closer to nearby nodes. This process results in a finalized feature map where the refined node patterns are presented in matrix form.

3.4. Extended SOM Approach

In this evaluation, the SOM approach functions as a tool to elucidate the range of IVT patterns that have historically been associated with extreme precipitation in the Upper Yuba watershed. Input data in this study is comprised of daily mean IVT for 260 extreme precipitation days over the region bounded by 15.5° and 65.5° north latitude and -105.75° and -170.25° west longitude. Given that IVT is a result of a combination of atmospheric conditions, such as wind speed and direction in the lower troposphere, pressure and geopotential height gradients, and regional baroclinicity, it can be thought of as a multivariate diagnostic, providing substantial meteorological information as input to the SOM algorithm (see *Appendix* for further discussion on IVT). The domain spanning

the US West Coast and North Pacific Ocean was chosen due to the well-established importance of enhanced corridors of IVT (ARs) over the North Pacific Ocean for driving heavy precipitation over the region (Dettinger et al., 2011).

To further capture the progression of IVT and associated synoptic conditions leading to extreme precipitation days, we implement an Extended SOM approach that provides daily mean IVT data for extreme precipitation days and the preceding four days over our study region as input to the SOM. In other words, the SOM is constructed with 260 (number of extreme precipitation days) five-day input vectors such that node assignment is based on conditions during the five days leading up to and including each extreme precipitation day. A five-day evaluation was selected to include relevant synoptic developments of extreme precipitation patterns while limiting irrelevant conditions that could be included with a longer time period. This new approach will strengthen the synoptic evaluation by clustering patterns with similar meteorological development and extreme precipitation conditions.

The MATLAB SOM Toolbox (https://www.cis.hut.fi/somtoolbox/) was used to perform the SOM algorithm. Input data for the SOM includes gridded IVT data over the study domain, which was first weighted by the square root of the cosine of latitude to account for variation in the data's grid cell area. After exploring results from a range of node numbers and matrix configurations, a 4×3 (12-node) SOM of 5-day patterns was chosen as an optimal SOM that captures pattern variability and limits pattern similarity. The SOM was first initialized with linearly fit IVT input data and then underwent an initial training run with a neighborhood radius of 4 and 100 iterations. A second run,

which begins with the final form of the initial training, was performed to further refine the final feature map with a reduced neighborhood radius of 1 and 2,000 iterations. The SOM Toolbox utilizes a ‘batch training’ algorithm, a fast and accurate form of training that does not require defining a ‘learning rate’ (Kohonen, 2005). SOM performance was evaluated through its quantization error and the use of a Sammon map (Fig. 3b), where the distances between nodes are presented 2-dimensionally (Sammon, 1969). A ‘flat’ map is indicative of good performance while a ‘twisted’ structure suggests poor SOM performance (Cassano et al., 2015; Gibson et al., 2017; Hewitson & Crane, 2002; Jaye et al., 2019).

4. Extended SOM Patterns

4.1. IVT Patterns

The Extended SOM output consists of twelve nodes of 5-day IVT patterns, which are difficult to visualize in the original 4 × 3 matrix, as each of the 12 nodes includes patterns for the extreme precipitation day and the four preceding days. Therefore, to illustrate the SOM in its original matrix, we present the Day 0 (the day of extreme precipitation) IVT patterns of each node in Figure 3a. The distances between the node patterns are presented in the 2-dimensional Sammon map space (Fig. 3b). The entire 5-day node patterns of the Extended SOM are presented in Figure 4 which are not shown in the original 4 × 3 orientation but instead as daily IVT patterns for the extreme precipitation day (Day 0) and the four preceding days (Day -1 to Day -4) of the nodes across each row. Here the IVT SOM pattern sequences, clustered based on the IVT pattern development over the five days, are shown in their entirety.

To describe the SOM, we will focus on the full Extended SOM results in Fig. 4. SOM node patterns show regions of enhanced IVT that develop over the North Pacific in the days leading up to extreme precipitation days with the moisture corridors typically making landfall on Day 0. Node patterns range from long, narrow IVT corridors that span the North Pacific throughout the five days (e.g. Node 10) to those exhibiting greater change and development of IVT across the days (e.g. Node 3). The range of 5-day patterns indicates a variety of meteorology, as represented by IVT, that leads to extreme precipitation in the Upper Yuba watershed.

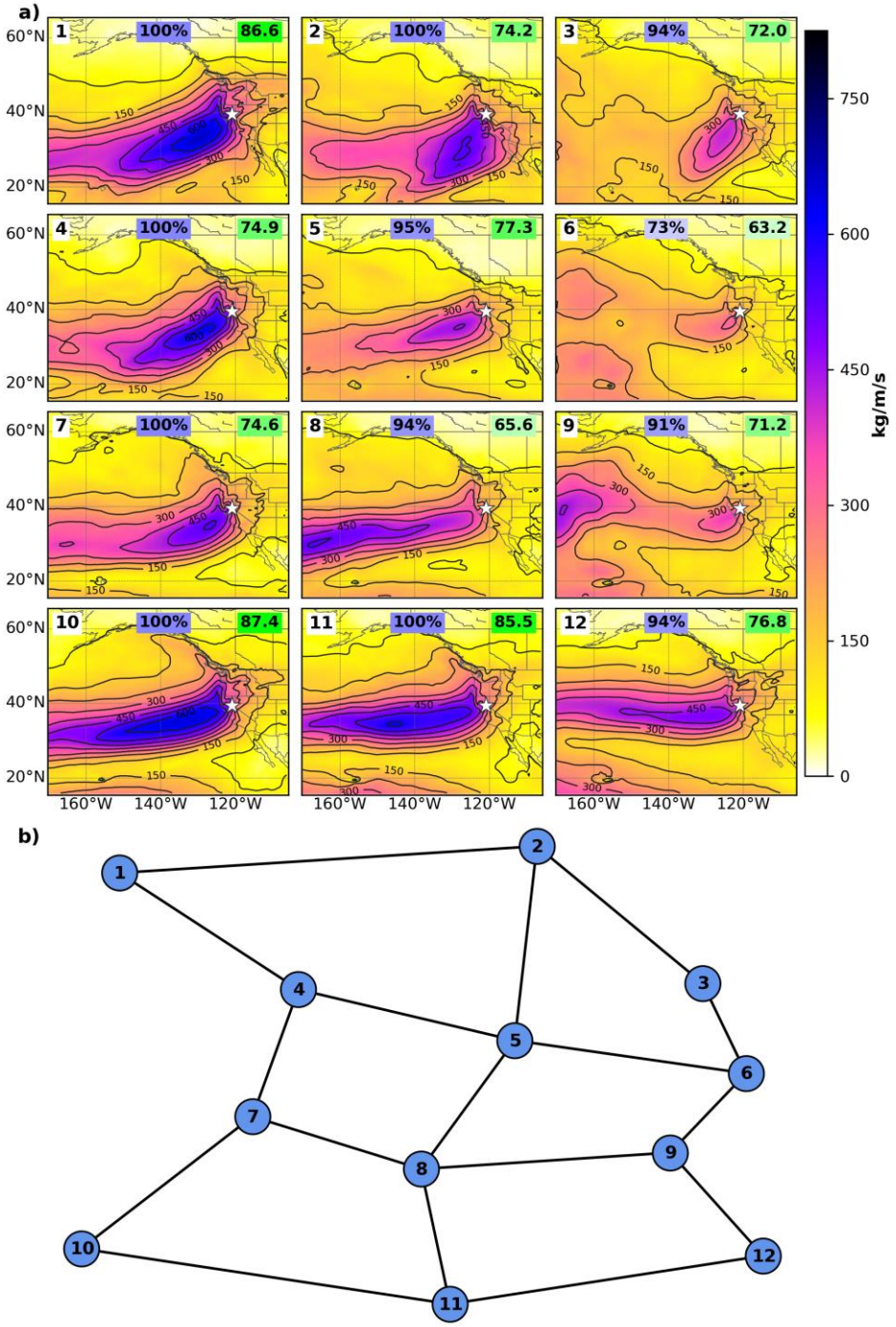

Figure 3. a) Partial results from a 12-node Extended SOM of daily IVT magnitude patterns (in kilograms per meter per second; shaded, contoured every 75 kg/m/s) for the Upper Yuba extreme precipitation days (Days 0 of the Extended SOM), with the node patterns shown in the SOM matrix form. Node numbers are marked in the upper lefthand corner of each panel, alongside the mean Day 0 watershed precipitation (in millimeters; in green) and the frequency of Day 0 AR activity (as a percentage; in blue) for the days assigned to each node. **b)** SOM Sammon map with the distances between nodes represented by the lines between node points, labeled by node number.

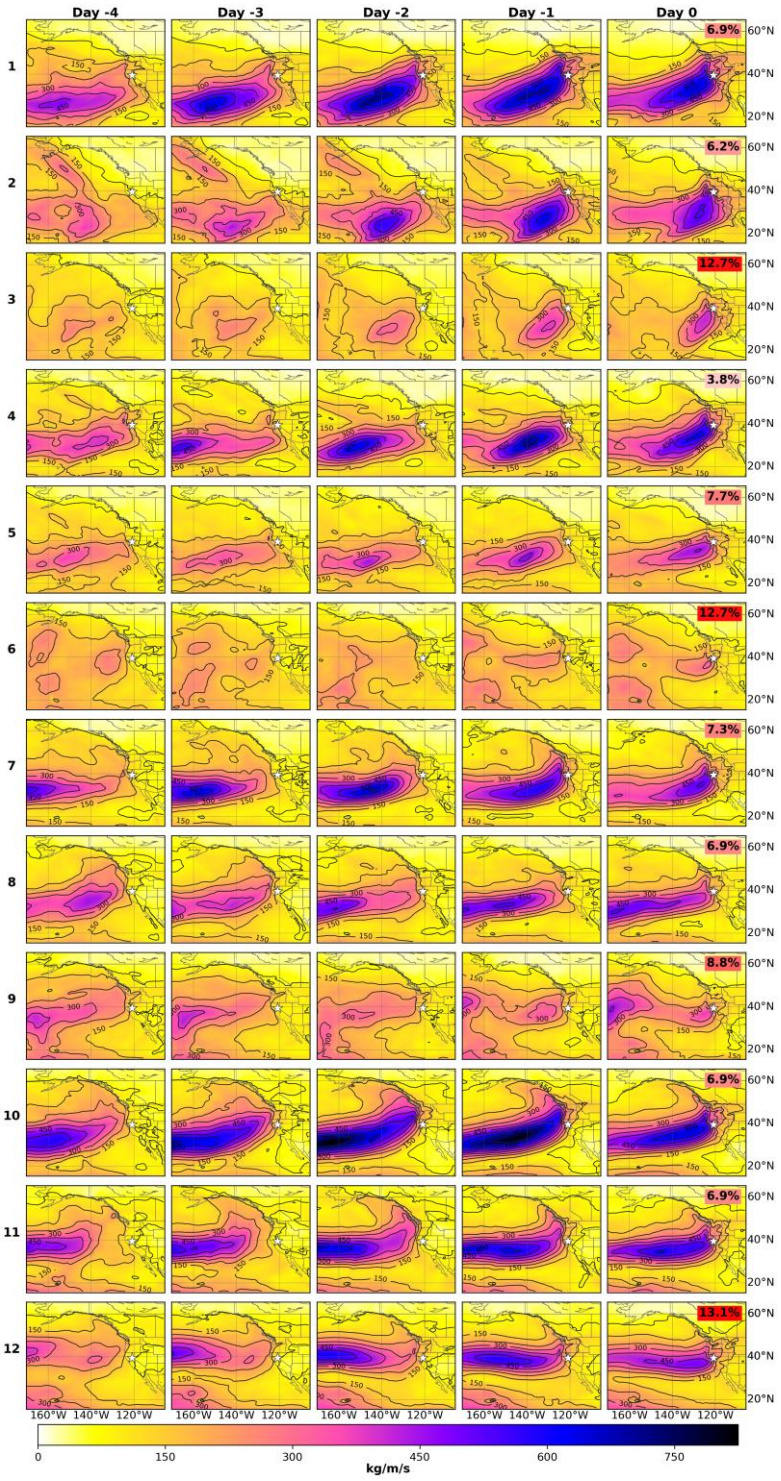

Figure 4. The full 5-day node patterns of a 12-node Extended SOM of daily IVT magnitude (in kilograms per meter per second; shaded, contoured every 75 kg/m/s) for Upper Yuba extreme precipitation days (Day 0) and the four preceding days (Days -1 to -4). Day 0 patterns are the same as those shown in matrix form in Fig. 3a. Node numbers are labeled on the left of each row. The percentage of all 5-day patterns assigned to each node is labeled in red on the Day 0 panels.

The IVT SOM patterns typically result in AR activity over the watershed, with AR frequency ranging from 73% to 100% of the extreme precipitation days across the nodes (Fig. 3a). Nodes 1 and 10 are the strongest patterns with the highest IVT magnitudes across the North Pacific (Fig. 4). AR activity is present 100% of the time during these nodes' Days 0 and the resulting watershed precipitation is greater than all other nodes (Fig. 3a). Node 1 and Node 10 make up less than 14% of Upper Yuba extreme precipitation days, which means while being intense and impactful, these systems are relatively infrequent. The 5-day IVT patterns of Nodes 1 and 10 also differ the most from other patterns as seen in the Sammon map in Fig. 3b, indicating that these nodes have distinct physical characteristics that differentiate them from other nodes. Both patterns show enhanced corridors of IVT present back to Day -4, which indicate large, zonally oriented systems such as a trans-Pacific AR. That said, these patterns differ as Node 10's IVT corridor is narrower with a more zonal orientation, while Node 1 is oriented more towards the northeast with high IVT values spanning much of the US West Coast.

Nodes 11 and 12 of the SOM show similar IVT patterns to Node 10, with strong zonally oriented IVT directed towards the watershed. Node 12 is the most common pattern, with 31 of the extreme days (13.1%) assigned to this node. This pattern results in AR activity 94% of the time and is characterized by a zonally oriented 'core' of enhanced IVT present on Day -4 that propagates towards the US West Coast from Days -3 to 0. This pattern is significantly weaker in IVT magnitude than the similar Node 10 but is nearly twice as common. Nodes 2–5 represent a different storm type characterized by

southerly to southwesterly orientated IVT and a more concentrated region of moisture. These patterns show strong development in IVT magnitude in the days leading up to extreme precipitation, perhaps most notably in Node 3 (Fig. 4). Nodes 6 and 9, two very similar nodes (Fig. 3b), show dramatically less water vapor across the North Pacific and little development of a moisture corridor. Node 6 has the weakest IVT pattern as well as the lowest mean precipitation and AR frequency of all nodes suggesting that these extreme days are often the result of other precipitation mechanisms.

4.2. Precipitation Patterns

The precipitation associated with each node pattern is further explored in Figure 5a through the precipitation frequency distributions of the days assigned to each node (histograms begin at the 90th percentile threshold, 51.53 mm). Mean precipitation is marked and labeled in green (the same as those listed in Fig. 3a) and median precipitation in magenta. About half of the node precipitation distributions reflect the larger precipitation distribution (Fig. 2) in that they are positively skewed (e.g. Node 6), while the others are closer to Gaussian (e.g. Node 10). Node 11 stands out as the only node with a distribution that does not include values near the 90th percentile threshold, indicating that these IVT patterns are not associated with lower-end extreme days. Alternatively, Node 6 consists entirely of days within the lower end of the upper decile, thus explaining both the high frequency (12.7%) and low precipitation (63.2 mm) associated with this pattern. The variety of precipitation distributions indicates the range of precipitation associated with each node pattern.

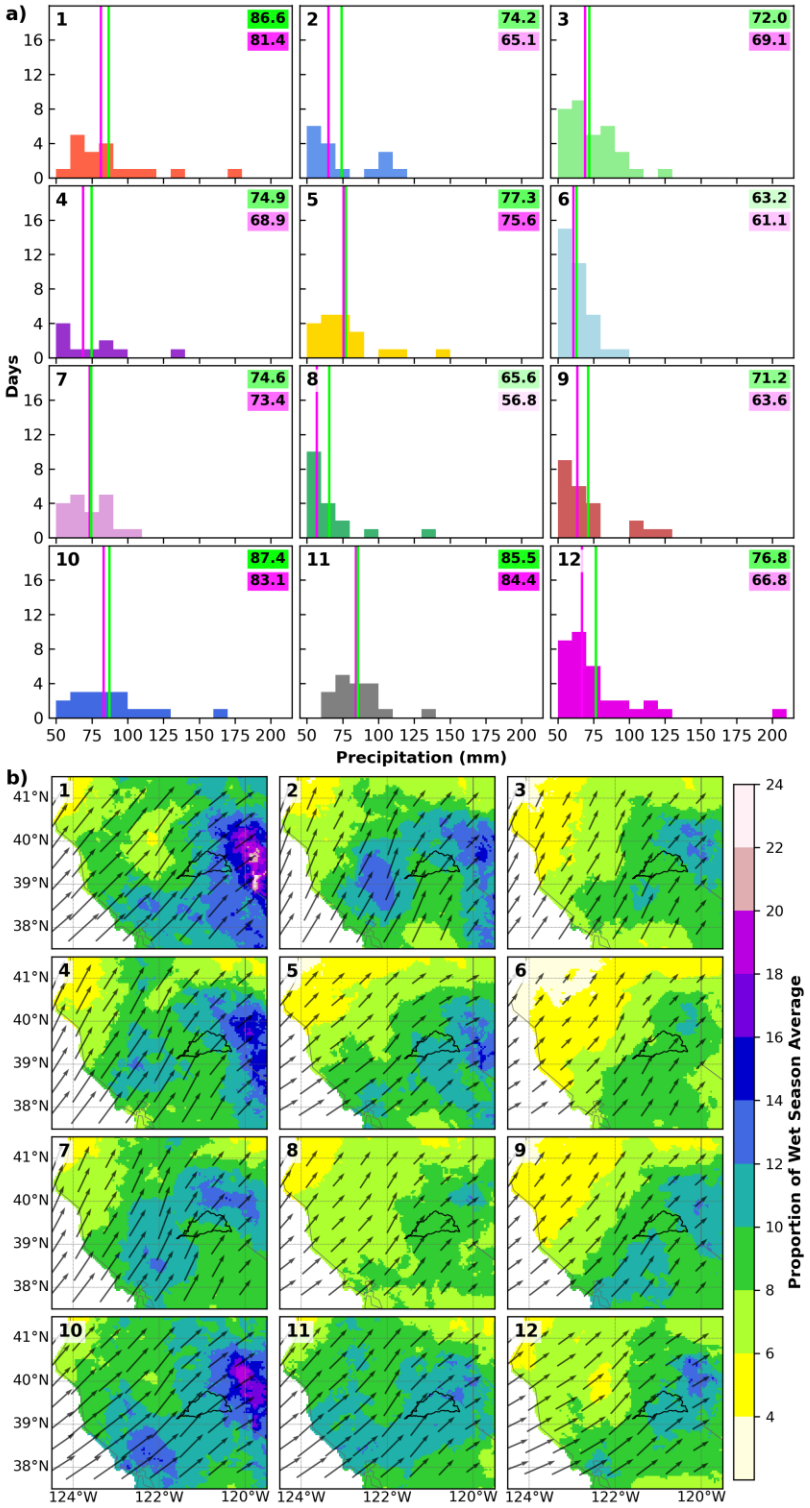

Figure 5. a) Precipitation distributions of Days 0 assigned to each node of the 12-node SOM, with the nodes' mean and median precipitation (in millimeters) marked and labeled in green and pink, respectively, and **b)** spatial precipitation anomaly patterns (as a proportion of the wet season mean) and daily mean IVT vectors across the Upper Yuba watershed and surrounding region.

When evaluating based on both mean and median precipitation, Nodes 1, 10, and 11 are the patterns capturing the heaviest precipitation days (Fig. 5a). These nodes are also characterized by the greatest moisture transport and strongest IVT corridors that are oriented southwest to northeast across the watershed. The node patterns resulting in the lowest precipitation are Nodes 6 and 8. Node 6 has the weakest IVT pattern with no strong corridor of moisture across the North Pacific, and Node 8, although a corridor is present, results in relatively low IVT magnitudes over the watershed. These results indicate the strong influence IVT magnitude has on extreme precipitation values over the Upper Yuba watershed as those with the greater IVT magnitude patterns result in the highest precipitation values.

In addition to evaluating the variation in mean precipitation, we also aim to understand the different spatial precipitation patterns within the watershed that can result from different IVT patterns. Figure 5b shows the spatial distribution of precipitation anomalies associated with days assigned to each node pattern, represented as a proportion of the mean wet season precipitation, alongside the node mean IVT vectors. Larger anomaly values indicate greater deviations from the typical wet season precipitation. Nodes 1 and 10, those with the strongest IVT patterns and greatest mean precipitation, unsurprisingly result in the largest precipitation anomalies across the watershed boundary. Precipitation anomalies associated with these nodes increase with elevation across the watershed and remain notably high east of the watershed boundary on the leeside of the Sierra Nevada. These strong IVT nodes likely lead to greater moisture availability and transport after the orographically-driven precipitation across the

mountain range. As a result, any additional moisture lift, perhaps due to a front or cold pool, results in precipitation falling across the dry region. Other nodes with high precipitation anomalies include Nodes 5, 11, and 12, which are all characterized as zonal IVT patterns. The IVT vectors across the watershed region show slight variations in IVT intensity and orientation over the region. Node 7 has strong southerly flow across the watershed, while Nodes 5 and 6 are examples of weak westerly flow. In general, however, IVT orientation across the nodes ranges very little and appears to have a weak influence on precipitation anomaly patterns.

4.3. Monthly Frequencies

Figure 6a shows the frequency of node assignments for the extreme precipitation days in each wet season month. Early winter months (October and November) experience a high percentage of Node 12 days (a weaker zonal flow pattern typically associated with AR activity), indicating favoring this pattern in the early season. Additionally, these early winter months experience fewer node types, which may be due to their lower frequency of extreme days (Fig. A1). October days are assigned only to Nodes 6 and 9 (~40%) and Nodes 11 and 12 (~60), which exist in the bottom right corner of the SOM space (Fig. 3b). November days include five additional patterns than October, also favoring nodes in the bottom right and center of the SOM. December most frequently experiences a Node 10 pattern, while the remaining months of January–March frequently experience Nodes 1, 3, and 6. Favored nodes during the earlier or later wet season may be indicative of different synoptic environments favoring specific IVT patterns. In this case, the wet season begins by favoring a weak and zonal IVT pattern, followed by the favoring of a

stronger and southwesterly IVT pattern. Lastly, the late winter and early spring favor patterns with a more southerly flow and tropical moisture transport.

In Figure 6b, the individual nodes' frequency distributions are shown, with the frequency noted as a percentage of days in each node. Some nodes occur much more frequently in certain months than others. Nodes 1 and 10, the two patterns with the greatest IVT (Fig. 4), are examples of this as Node 1 occurs most often in February while Node 10 is dominated by December occurrences. Despite both being extreme patterns resulting in high mean watershed precipitation, these nodes differ in both IVT characteristics and when they most frequently occur, which may be indicative of distinct synoptic conditions driving these two pattern types. Nodes 9, 11, and 12 occur more frequently in the first half of the wet season and become less common in the later three months while Node 3 becomes more frequent as the wet season progresses. This suggests that certain nodes are favored in the earlier and later winter months.

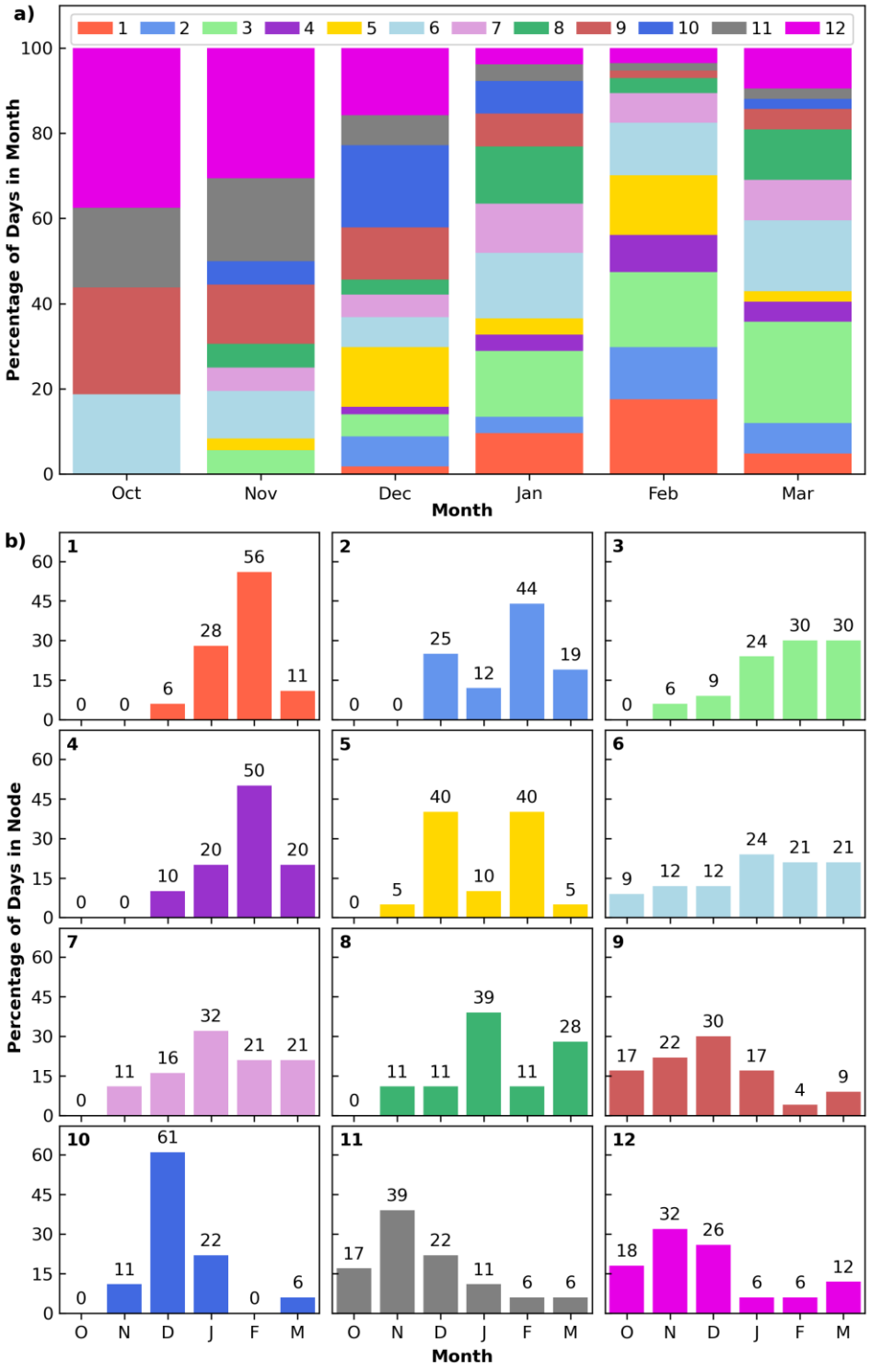

Figure 6. a) Node frequencies for each wet season month of October through March as a percentage of extreme precipitation days in each month and **b)** monthly frequencies for each node pattern as a percentage of extreme precipitation days in each node.

4.4. Annual Frequencies

Considerable year-to-year variability exists in the number of extreme precipitation days and node assignments across the 42-year climatology, with no apparent trend in either extreme precipitation day or node pattern frequency (Fig. 7). The 2016–17 water year had the most extreme precipitation days (18) while the 2000–01 year did not have any. Most water years consist of a variety of node assignments, including 1999–2000 where each extreme precipitation day has a different node assignment. Favoring of certain node assignments, however, does occur in other years including 2003–04 and 2005–06 where over half of the extreme precipitation days are assigned to Node 1.

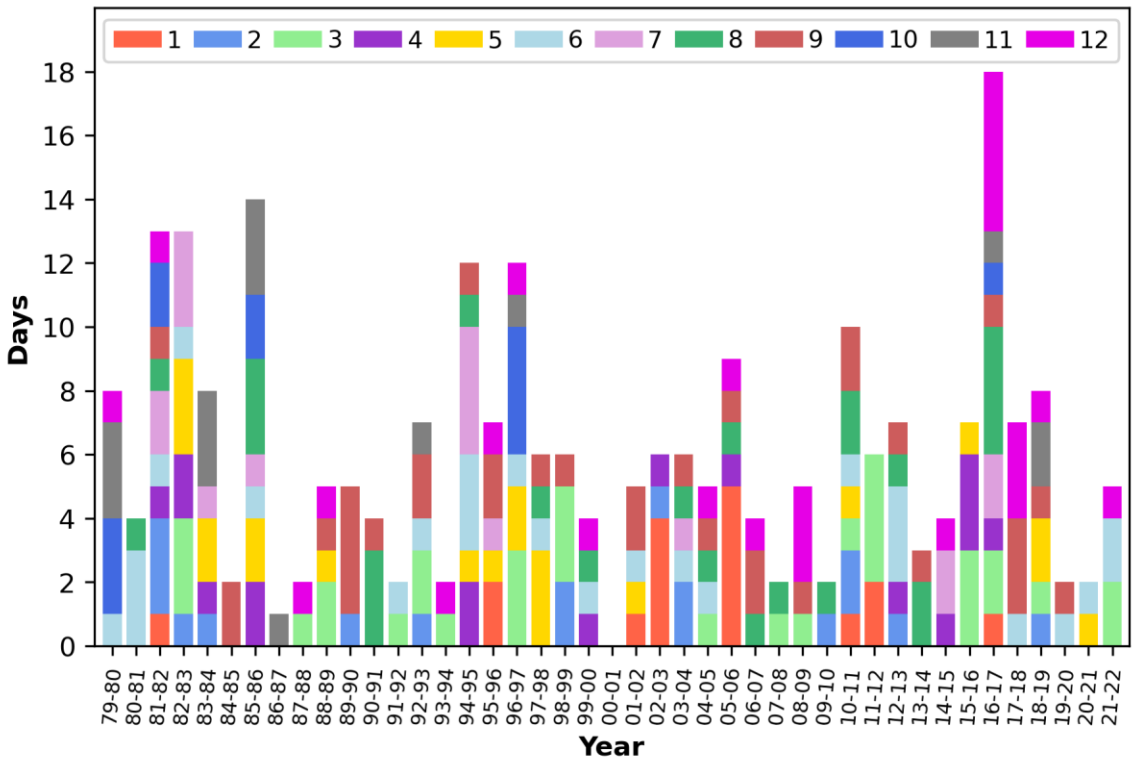

Figure 7. Node assignments for each extreme precipitation day across the climatological period from 1980 to 2021, grouped by water year (defined as October through March). The 79–80 and 21–22 water years are limited to 1980 and 2021 days, respectively.

5. Synoptic Evaluation

Figures 8–13 further evaluate the synoptic conditions associated with six of the 12 SOM nodes, which were selected to represent the range of synoptic and dynamic characteristics in the SOM. The other six nodes are included in the supplemental material (Figs. A3–A8). In Fig. 8, the Node 1 IVT SOM pattern is shown alongside composites of 300 hPa wind speed and Z300 anomalies, SLP and SLP anomalies, and 850 hPa temperature anomalies and wind vectors for days assigned to Node 1.

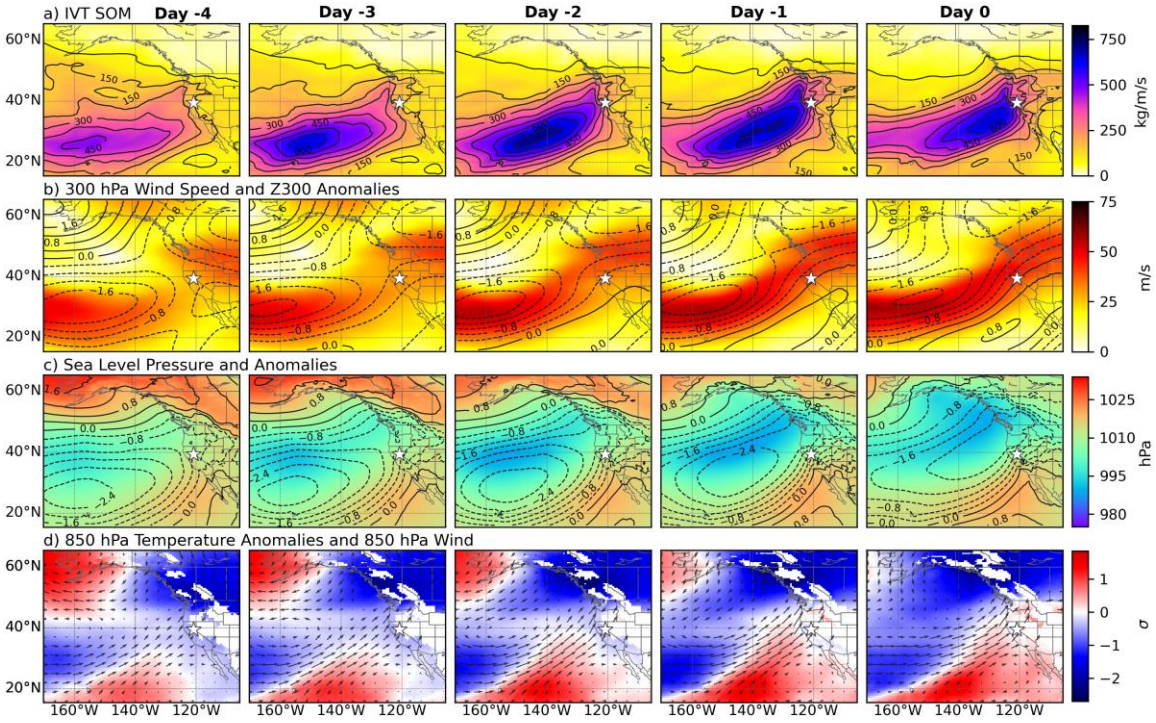

Figure 8. Synoptic pattern composites for the days assigned to Node 1, with the **a)** IVT SOM pattern, as shown in Fig. 4; **b)** 300 hPa wind speed (shaded in meters per second) and 300 hPa geopotential height anomalies (contoured every 0.4 standard deviations); **c)** sea level pressure (shaded in hectopascals) and sea level pressure anomalies (contoured every 0.4 standard deviations); and **d)** 850 hPa temperature anomalies (shaded in standard deviations) and 850 hPa wind (in vectors).

300 hPa winds co-align with the region of enhanced IVT with simultaneous strengthening of IVT and wind speeds throughout the five days. A double Z300 anomaly low north of positive Z300 anomalies results in upper-level southwesterly flow (Fig. 8b) and a very strong temperature gradient between positive and negative temperature anomalies near the surface (850 hPa), indicating the likely presence of a cold front on Node 1 days (Fig. 8d). Anomalously low SLP offshore of the watershed region leads to a strong pressure gradient promoting the transport of low-level moisture into the watershed (Fig. 8c). Strong warm air advection occurs in the watershed in the days leading up to Day 0 as air is transported northward by low-level winds, evident at 850 hPa. These synoptic conditions support strong advection of low-level warm and moist air northeastward ahead of a cold front associated with an extratropical cyclone.

Node 3 is characterized by a very different meteorological progression than Node 1, with evidence of a strengthening surface cyclone progressing eastward from Day -4 to Day 0 (Fig. 9). IVT is relatively weak across the North Pacific on Day -4 and gradually strengthens alongside the development of a surface low-pressure system and Z300 anomaly low. Negative low-level temperature anomalies across the North Pacific also intensify during the 5-day sequence, with the most negative temperature anomalies co-occurring with the positively tilted Z300 anomalies. The resulting conditions consist of a surface low (Fig. 9c) and cyclonic 850 hPa wind pattern (Fig. 9d), which promote moisture advection and dynamic lift of the cold air over the watershed. Altogether, days assigned to Node 3 are associated with cyclogenesis before the landfall of the developed surface cyclone.

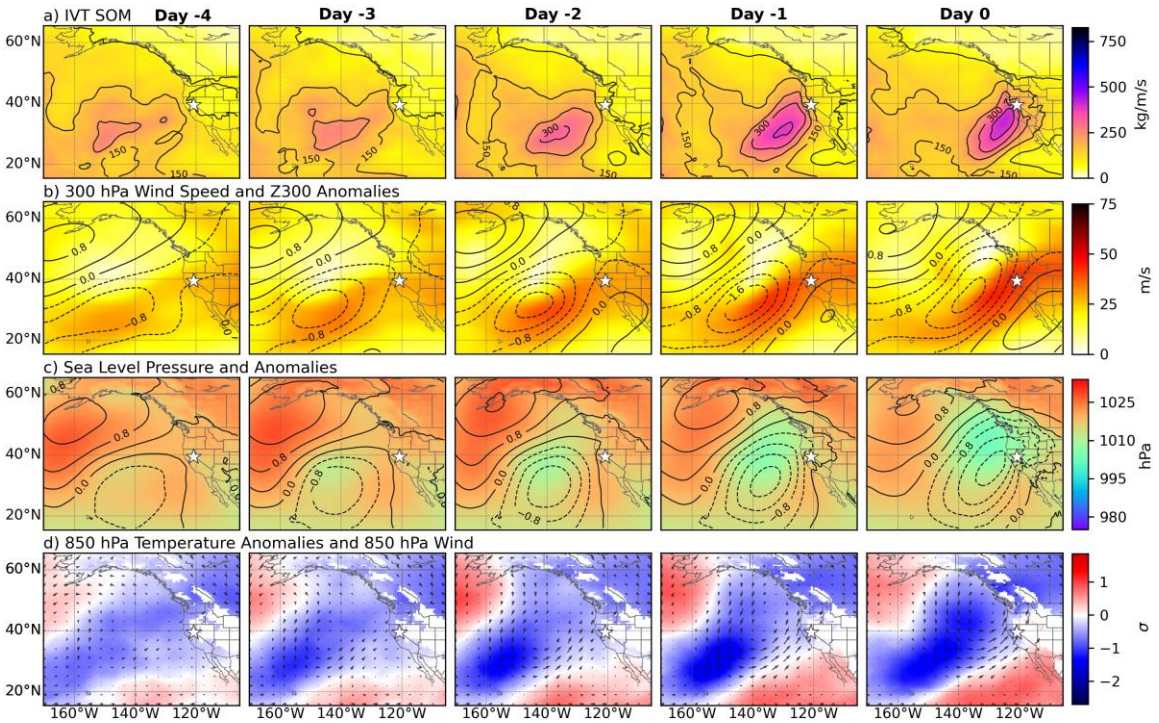

Figure 9. As in Fig. 8 but for Node 3.

Node 5 is characterized by weak flow across the North Pacific with the transport of an IVT core that reaches the coastline on Day 0 (Fig. 10). The resulting landfalling moisture corridor is zonally oriented with slight cyclonic circulation in both the upper and lower levels. Jet stream winds and Z300 anomalies are weaker than other node patterns, as is the low-pressure system associated with the node's moisture transport (Fig. 10b and c). 850 hPa winds strengthen slightly alongside the development of the SLP low leading to zonal low-level flow across the North Pacific between positive and negative temperature anomalies. Southwesterly to southerly near-surface flow around the coastline is somewhat misaligned with the IVT orientation, suggesting the IVT corridor is being influenced by winds at higher altitudes. Negative 850 hPa temperature anomalies span California in association with the low pressure at the surface and aloft throughout the 5-

day sequence. Overall, Node 5 has relatively weak flow at the lower and higher levels, although the moderately strengthening low-level winds and IVT supply moisture and cool air to the watershed.

Node 6 days are characterized by weak IVT across the North Pacific and relatively low watershed precipitation amounts (Fig. 3a). An east-west Z300 anomaly dipole develops throughout the five days resulting in an upper-level wind pattern that doesn't promote the zonal or southwesterly flow seen in other patterns, but instead anticyclonic and cyclonic circulation around the high and low anomalies (Fig. 11b). Underneath the Z300 negative anomaly, negative SLP anomalies strengthen to the north of the watershed, centered over the Pacific Northwest (Fig. 11c). Cyclonically circulating 850 hPa winds strengthen throughout the 5-day pattern transporting cooler air from higher latitudes to the watershed. These strong negative temperature anomalies indicate that Node 6 events are colder than many of the other nodes and would be more likely to bring significant snowfall to the watershed and Sierra Nevada mountains.

Similar atmospheric characteristics to Node 6 occur in Node 9 (Fig. A7), although slight variations in conditions result in higher mean precipitation in Node 9. A similarly strong Z300 anomaly dipole develops in Node 9, yet the pattern occurs at lower latitudes and has stronger winds and gradients between high and low SLP anomalies, likely enhancing the moisture transport and precipitation associated with this node. IVT in these patterns remains relatively low and the associated precipitation may be driven by other mechanisms such as a cold front, cyclogenesis, or convection, although further investigation is outside the scope of this evaluation.

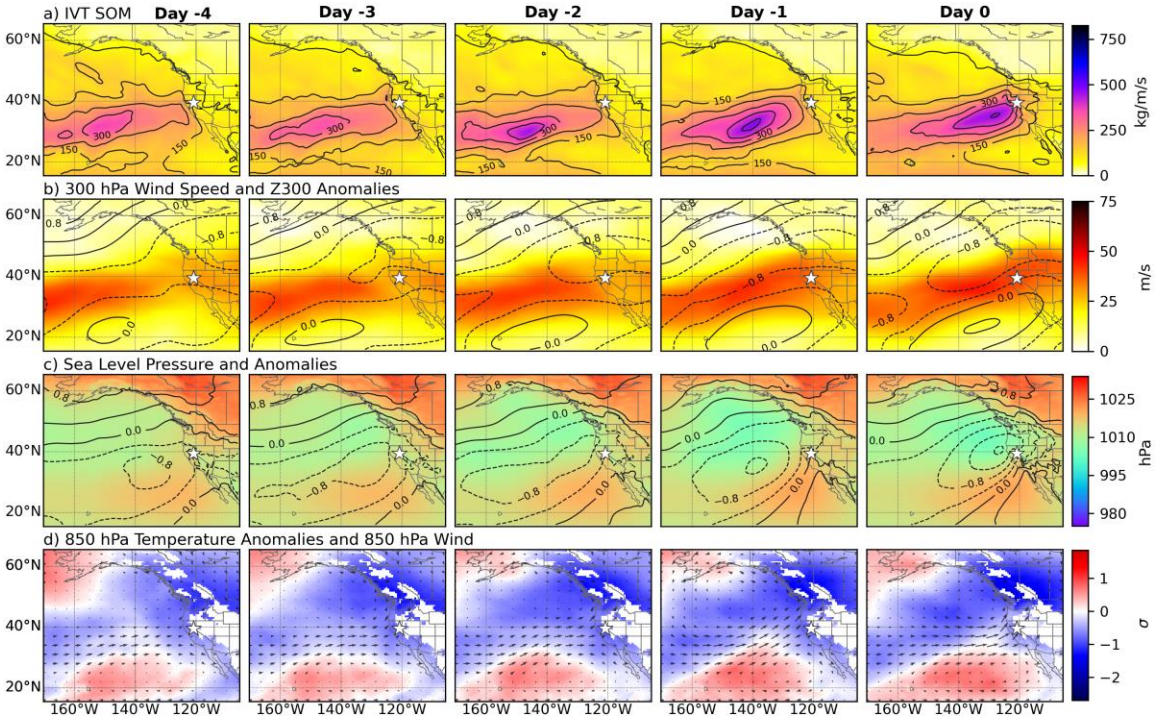

Figure 10. As in Fig. 8 but for Node 5.

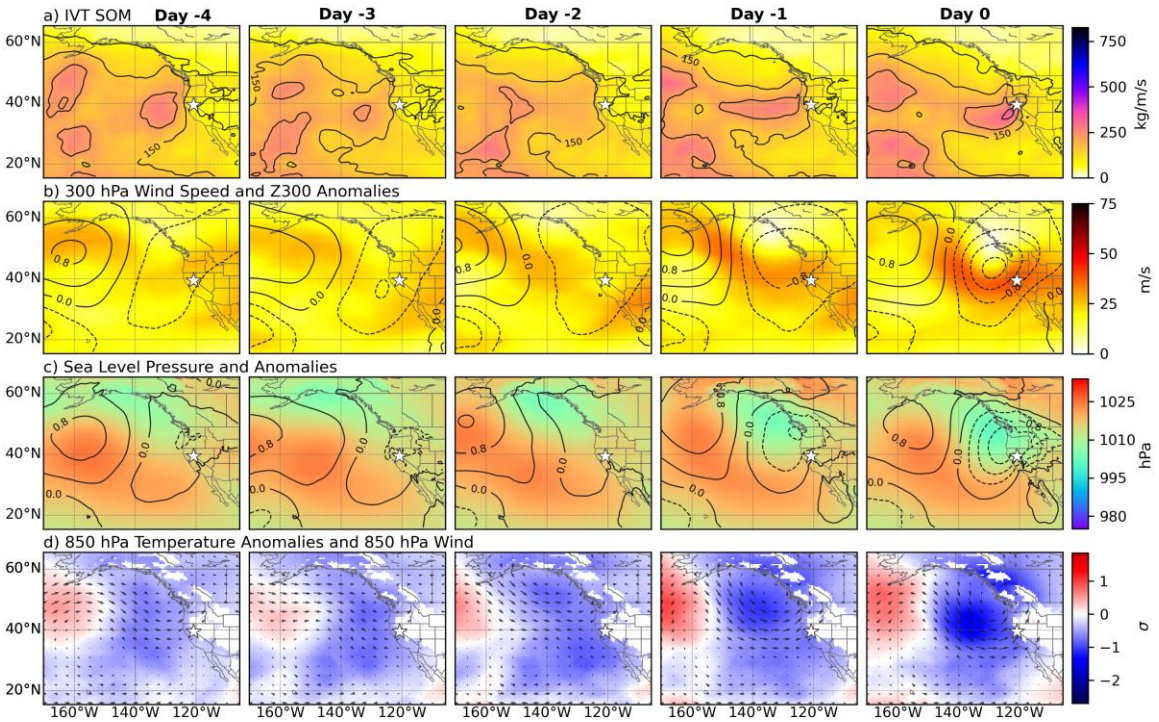

Figure 11. As in Fig. 8 but for Node 6.

Node 10 has the strongest IVT corridor of all nodes and is associated with the deepening of a large low-pressure system over the northeast Pacific and strong upper and lower-level winds (Fig. 12). The development of a north-south Z300 anomaly dipole promotes relatively strong Z300 zonal winds coinciding spatially with the IVT corridor, which appears to source its moisture from the subtropics (Fig. 12a and b). North of the 300 hPa jet, SLP decreases with a low-pressure system strengthening southeast of Alaska. An SLP anomaly gradient develops in the same region as the enhanced IVT and upper-level wind patterns. Low-level winds are strong both within the IVT corridor but also across much of the Northeast Pacific, with the rapid movement of near-surface air contributing to the transport of warm air resulting in positive temperature anomalies across California (Fig. 12d). More than the other nodes, the meteorology associated with Node 10 is representative of a 'Pineapple Express' AR, with strong transport of subtropical moisture at all levels, driven by a deep surface low south of Alaska.

In Node 12, the jet stream strengthens over the 5-day sequence, resulting in strong cyclonic flow and a deep trough at 300 hPa (Fig. 13). Low-level winds follow a similar northwesterly flow, contributing to the transport of cold air into the region. Contrary to many of the other nodes, the corridor of enhanced IVT is not as closely spatially aligned with the strong upper-level winds or the gradient between the SLP anomalies but instead is quite zonal. This node has relatively weaker moisture transport than most yet is the most frequently occurring node.

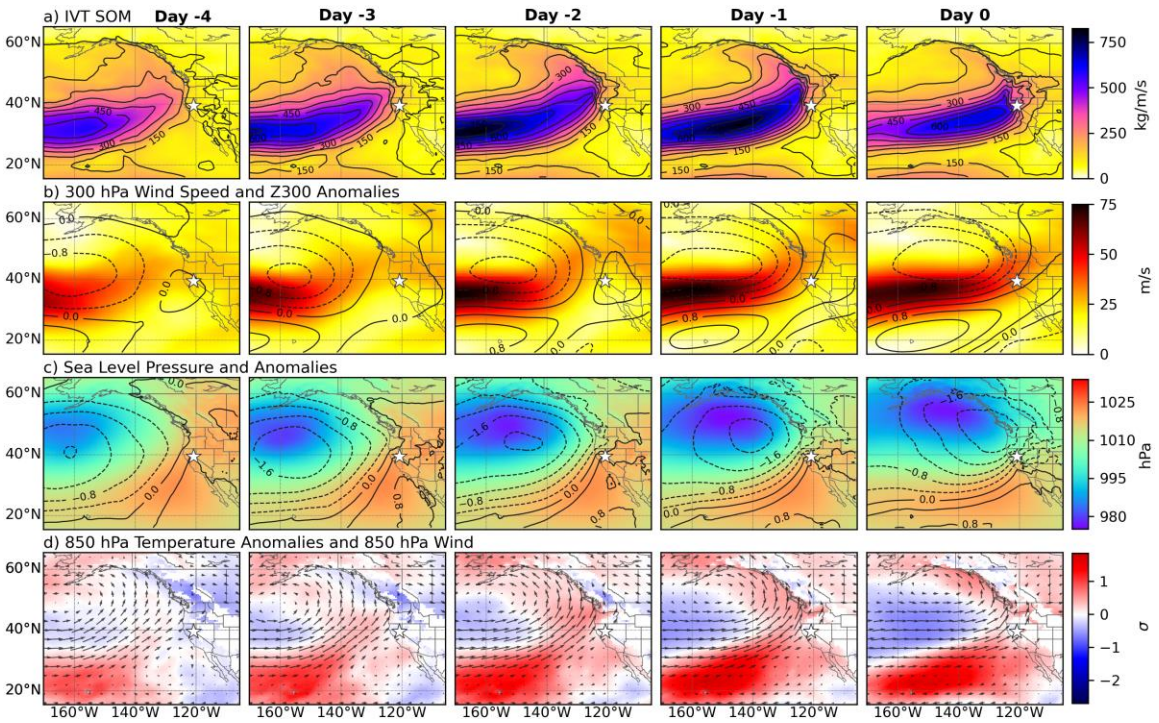

Figure 12. As in Fig. 8 but for Node 10.

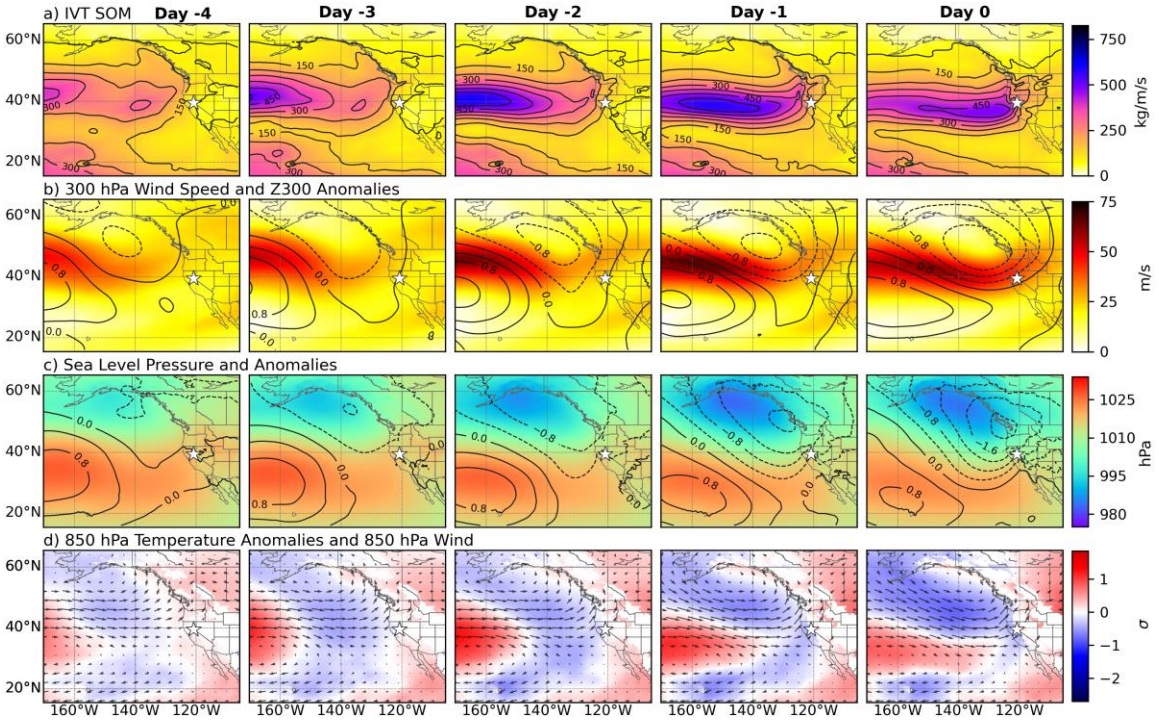

Figure 13. As in Fig. 8 but for Node 12.

6. Conclusions and Discussion

In this study, we aim to evaluate the range of meteorological patterns responsible for extreme precipitation in the Upper Yuba watershed – a historically flood-prone region that remains challenging to forecast due to its complex terrain and orographically enhanced AR-driven precipitation. We introduce and apply a novel 5-day 'Extended SOM' approach that utilizes the synoptic patterns of extreme precipitation days alongside the four preceding days to cluster patterns based on the synoptic and dynamic development leading up to extreme days. The key takeaways of the study are as follows:

1) Extreme precipitation in the Upper Yuba watershed is driven by a broad range of synoptic patterns and driving mechanisms which can be clustered, presented, and evaluated using an IVT SOM.
2) Many of these extreme precipitation patterns are associated with strong moisture transport over the North Pacific that results in AR activity across the watershed, although the intensity of IVT and frequency of ARs vary across patterns.
3) Nodes 6 and 9 are unique in that they drive extreme precipitation without the presence of strong IVT, indicating the importance of other mechanisms driving or enhancing precipitation in these nodes.
4) Precipitation amounts for each pattern tend to be driven by IVT intensity; patterns that promote the northward transport of warm and moist tropical air produce the greatest watershed precipitation.

Several different meteorological patterns result in extreme precipitation over the watershed and are largely characterized by enhanced moisture transport resulting in a narrow corridor of southerly to southwesterly IVT associated with a surface low-pressure system. The orientation and intensity of such patterns as well as the associated synoptic conditions result in a collection of unique storms that impact the region and result in extreme precipitation. The most frequent node consists of relatively weak zonal flow that promotes the transport of northwesterly air toward the watershed leading to cooler-than-average conditions. Contrarily, the least common pattern has strong southwesterly flow and negative SLP anomalies promoting strong moisture transport from the subtropics.

Nodes with the greatest IVT magnitude and those promoting the transport of subtropical air were associated with the highest watershed precipitation. Patterns with strong zonal flow are favored earlier in the season and those promoting cyclogenesis and southwesterly flow are favored in the later wet season months. AR activity occurs in all node types indicating the importance of these systems in driving regional precipitation. Nodes 6 and 9 have the fewest AR days and relatively low IVT, suggestive of additional mechanisms promoting extreme precipitation in these storm types. These two nodes account for a notable portion of extreme precipitation days (21.5%; Fig. 4) and because they do not show clear AR activity, may not be properly recognized as extreme storms and forecasted inaccurately.

The Extended SOM methodology proves useful in clustering patterns with similar synoptic patterns, although there may be limitations to this approach. For example, the Extended SOM considers each day of the 5-day patterns equally, meaning Days -4 are

just as influential as Days 0 in clustering. This may lead to patterns with similar preconditions and less similar final conditions assigned to the same node. This, however, may not be an issue as patterns near extreme precipitation days tend to have the greatest IVT magnitude and could result in these strong IVT patterns greater influencing the SOM clustering. Further investigation into how this type of training impacts node clustering could determine the importance of such limitations.

In conclusion, a wide array of synoptic patterns results in extreme precipitation across the Upper Yuba watershed, with the warm and moist systems resulting in the greatest precipitation across the watershed. That said, patterns associated with less moisture transport still result in extreme precipitation across the region, suggesting that there is variation in the meteorological drivers of regional extreme precipitation. Such evaluation of the range of atmospheric conditions resulting in extremes could prove useful in improving the forecasting of extreme events. The clustering of atmospheric patterns based on a 5-day synoptic development can contribute to the classifying and understanding of storm types and their development that lead to extreme precipitation and can be expanded to the exploration and evaluation of other extreme weather events across the globe.

References

Abatzoglou, J. T. (2013). Development of gridded surface meteorological data for ecological applications and modelling. *International Journal of Climatology*, *33*(1), 121–131. https://doi.org/10.1002/joc.3413

Aragon, C. M., Loikith, P. C., McCullar, N., & Mandilag, A. (2020). Connecting local-scale heavy precipitation to large-scale meteorological patterns over Portland, Oregon. *International Journal of Climatology*, *40*(11), 4763–4780. https://doi.org/10.1002/joc.6487

Barlow, M., Gutowski, W. J., Gyakum, J. R., Katz, R. W., Lim, Y.-K., Schumacher, R. S., Wehner, M. F., Agel, L., Bosilovich, M., Collow, A., Gershunov, A., Grotjahn, R., Leung, R., Milrad, S., & Min, S.-K. (2019). North American extreme precipitation events and related large-scale meteorological patterns: A review of statistical methods, dynamics, modeling, and trends. *Climate Dynamics*, *53*(11), 6835–6875. https://doi.org/10.1007/s00382-019-04958-z

Barth, N. A., Villarini, G., & Nayak, M. A. (2015). Mixed populations and annual flood frequency estimates in the western United States: The role of atmospheric rivers. *Water Resources Research, 53*(1), 257-269. https://doi.org/10.1002/2016wr019064

Cannon, F., Hecht, C. W., Cordeira, J. M., & Ralph, F. M. (2018). Synoptic and Mesoscale Forcing of Southern California Extreme Precipitation. *Journal of Geophysical Research*, *123*(24). https://doi.org/10.1029/2018jd029045

Cassano, E. N., Glisan, J. M., Cassano, J. J., Gutowski, W. J., & Seefeldt, M. W. (2015). Self-organizing map analysis of widespread temperature extremes in Alaska and Canada. *Climate Research*, *62*(3), 199–218. doi: 10.3354/cr01274.

Cordeira, J. M., Stock, J., Dettinger, M. D., Young, A. M., Kalansky, J. F., & Ralph, F. M. (2019). A 142-Year Climatology of Northern California Landslides and Atmospheric Rivers. *Bulletin of the American Meteorological Society*, *100*(8), 1499–1509. https://doi.org/10.1175/BAMS-D-18-0158.1

Corringham, T. W., Ralph, F. M., Gershunov, A., Cayan, D. R., & Talbot, C. A. (2019). Atmospheric rivers drive flood damages in the western United States. *Science Advances*, *5*(12). https://doi.org/10.1126/sciadv.aax4631

Daly, C., Neilson, R. P., & Phillips, D. L. (1994). A Statistical-Topographic Model for Mapping Climatological Precipitation over Mountainous Terrain. *Journal of Applied Meteorology and Climatology*, *33*(2), 140–158. https://doi.org/10.1175/1520-0450(1994)033<0140:ASTMFM>2.0.CO;2

Dettinger, M. D. (2013). Atmospheric Rivers as Drought Busters on the U.S. West Coast. *Journal of Hydrometeorology*, *14*(6), 1721–1732. https://doi.org/10.1175/JHM-D-13-02.1

Dettinger, M. D., Ralph, F. M., Ralph, F. M., Das, T., Neiman, P. J., & Cayan, D. R. (2011). Atmospheric Rivers, Floods and the Water Resources of California. *Water*, *3*(2), 445–478. https://doi.org/10.3390/w3020445

Fernandes, L. G., & Loikith, P. C. (2024). Does El Niño affect MJO-AR connections over the North Pacific and associated North American precipitation? *Climate Dynamics*. https://doi.org/10.1007/s00382-024-07177-3

Fridirici, R., & Shelton, M. L. (2000). Natural and Human Factors in Recent Central Valley Floods. *Yearbook of the Association of Pacific Coast Geographers*, *62*, 53–69. http://dx.doi.org/10.1353/pcg.2000.0004

Gelaro, R., McCarty, W., Suárez, M. J., Todling, R., Molod, A., Takacs, L., Randles, C. A., Darmenov, A., Bosilovich, M. G., Reichle, R., Wargan, K., Coy, L., Cullather, R., Draper, C., Akella, S., Buchard, V., Conaty, A., Silva, A. M. da, Gu, W., … Zhao, B. (2017). The Modern-Era Retrospective Analysis for Research and Applications, Version 2 (MERRA-2). *Journal of Climate*, *30*(14), 5419–5454. https://doi.org/10.1175/JCLI-D-16-0758.1

Gibson, P. B., Perkins-Kirkpatrick, S. E., Uotila, P., Pepler, A. S., & Alexander, L. V. (2017). On the use of self-organizing maps for studying climate extremes. *Journal of Geophysical Research: Atmospheres*, *122*(7), 3891–3903. https://doi.org/10.1002/2016JD026256

Guan, B., & Waliser, D. E. (2015). Detection of atmospheric rivers: Evaluation and application of an algorithm for global studies. *Journal of Geophysical Research: Atmospheres*, *120*(24), 12514–12535. https://doi.org/10.1002/2015JD024257

Guan, B., & Waliser, D. E. (2019). Tracking Atmospheric Rivers Globally: Spatial Distributions and Temporal Evolution of Life Cycle Characteristics. *Journal of Geophysical Research: Atmospheres*, *124*(23), 12523–12552. https://doi.org/10.1029/2019JD031205

Guan, B., Waliser, D. E., & Ralph, F. M. (2018). An Intercomparison between Reanalysis and Dropsonde Observations of the Total Water Vapor Transport in Individual Atmospheric Rivers. *Journal of Hydrometeorology*, *19*(2), 321–337. https://doi.org/10.1175/JHM-D-17-0114.1

Guirguis, K., Gershunov, A., Clemesha, R. E. S., Tamara Shulgina, Shulgina, T., Subramanian, A. C., & Ralph, F. M. (2018). Circulation Drivers of Atmospheric Rivers at the North American West Coast. *Geophysical Research Letters*, *45*(22), 12576–12584. https://doi.org/10.1029/2018gl079249

Harris, S. M., & Carvalho, L. M. V. (2018). Characteristics of southern California atmospheric rivers. *Theoretical and Applied Climatology*, *132*(3), 965–981. https://doi.org/10.1007/s00704-017-2138-1

Hecht, C. W., & Cordeira, J. M. (2017). Characterizing the influence of atmospheric river orientation and intensity on precipitation distributions over North Coastal California. *Geophysical Research Letters*, *44*(17), 9048–9058. https://doi.org/10.1002/2017gl074179

Hewitson, B. C., & Crane, R. G. (2002). Self-organizing maps: Applications to synoptic climatology. *Climate Research*, *22*(1), 13–26. https://doi.org/10.3354/cr022013

Jaye, A. B., Bruyère, C. L., & Done, J. M. (2019). Understanding future changes in tropical cyclogenesis using Self-Organizing Maps. *Weather and Climate Extremes*, *26*, 100235. https://doi.org/10.1016/j.wace.2019.100235

Kim, J., Waliser, D. E., Neiman, P. J., Guan, B., Ryoo, J.-M., & Wick, G. A. (2013). Effects of atmospheric river landfalls on the cold season precipitation in California. *Climate Dynamics*, *40*(1), 465–474. https://doi.org/10.1007/s00382-012-1322-3

Kohonen, T. (1982). Self-organized formation of topologically correct feature maps. *Biological Cybernetics*, *43*(1), 59–69. https://doi.org/10.1007/BF00337288

Kohonen, T. (2005, March 18). *The Self-Organizing Map (SOM)*. https://www.cis.hut.fi/somtoolbox/theory/somalgorithm.shtml

Lamjiri, M. A., Dettinger, M. D., Ralph, F. M., Ralph, F. M., & Guan, B. (2017). Hourly storm characteristics along the U.S. West Coast: Role of atmospheric rivers in extreme precipitation. *Geophysical Research Letters*, *44*(13), 7020–7028. https://doi.org/10.1002/2017gl074193

Lavers, D. A., Waliser, D. E., Ralph, F. M., & Dettinger, M. D. (2016). Predictability of horizontal water vapor transport relative to precipitation: Enhancing situational awareness for forecasting western U.S. extreme precipitation and flooding. *Geophysical Research Letters*, *43*(5), 2275–2282. https://doi.org/10.1002/2016gl067765

Liu, Y., Weisberg, R. H., Liu, Y., & Weisberg, R. H. (2011). A Review of Self-Organizing Map Applications in Meteorology and Oceanography. In *Self Organizing Maps—Applications and Novel Algorithm Design*. IntechOpen. https://doi.org/10.5772/13146

Loikith, P. C., Lintner, B. R., & Sweeney, A. (2017). Characterizing Large-Scale Meteorological Patterns and Associated Temperature and Precipitation Extremes over the Northwestern United States Using Self-Organizing Maps. *Journal of Climate*, *30*(8), 2829–2847. https://doi.org/10.1175/JCLI-D-16-0670.1

Luković, J., Chiang, J. C. H., Blagojević, D., & Sekulić, A. (2021). A Later Onset of the Rainy Season in California. *Geophysical Research Letters*, *48*(4), e2020GL090350. https://doi.org/10.1029/2020GL090350

Moore, B. J., White, A. B., Gottas, D. J., & Neiman, P. J. (2020). Extreme Precipitation Events in Northern California during Winter 2016─17: Multiscale Analysis and Climatological Perspective. *Monthly Weather Review*, *148*(3), 1049–1074. https://doi.org/10.1175/mwr-d-19-0242.1

Neiman, P. J., Ralph, F. M., Wick, G. A., Lundquist, J. D., & Dettinger, M. D. (2008). Meteorological Characteristics and Overland Precipitation Impacts of Atmospheric Rivers Affecting the West Coast of North America Based on Eight

Years of SSM/I Satellite Observations. *Journal of Hydrometeorology*, *9*(1), 22–47. https://doi.org/10.1175/2007JHM855.1

Ohara, N., Kavvas, M. L., Anderson, M. L., Chen, Z. Q., & Ishida, K. (2017). Characterization of Extreme Storm Events Using a Numerical Model–Based Precipitation Maximization Procedure in the Feather, Yuba, and American River Watersheds in California. *Journal of Hydrometeorology*, *18*(5), 1413–1423. https://doi.org/10.1175/jhm-d-15-0232.1

Pörtner, H.-O., Roberts, D. C., Adelekan, I., Adler, C., Adrian, R., Aldunce, P., Ali, E., Ara Begum, R., Bednar-Friedl, B., Bezner Kerr, R., Biesbroek, R., Birkmann, J., Bowen, K., Caretta, M.A., Carnicer, J., Castellanos, E., Cheong, T.S., Chow, W., Cissé, G., … Zaiton Ibrahim, Z. (2022). Technical Summary (Pörtner, H.-O., Roberts, D.C., Poloczanska, E.S., Mitenbeck, K., Tignor, M., Alegría, A., Craig, M., Langsdorf, S., Löschke, S., Möller, V., & Okem, A., Eds.). In Pörtner, H.-O., Roberts, D.C., Tignor, M., Poloczanska, E.S., Mitenbeck, K., Alegría, A., Craig, M., Langsdorf, S., Löschke, S., Möller, V., Okem, A., & Rama, B (Eds.), *Climate Change 2022: Impacts, Adaptation and Vulnerability. Contribution of Working Group II to the Sixth Assessment Report of the Intergovernmental Panel on Climate Change* (pp. 37–118). Cambridge University Press, Cambridge, UK and New York, NY, USA. doi:10.1017/9781009325844.002.

Ralph, F. M., Neiman, P. J., & Rotunno, R. (2005). Dropsonde Observations in Low-Level Jets over the Northeastern Pacific Ocean from CALJET-1998 and PACJET-2001: Mean Vertical-Profile and Atmospheric-River Characteristics. *Monthly Weather Review*, *133*(4), 889–910. https://doi.org/10.1175/mwr2896.1

Ralph, F. M., Neiman, P. J., & Wick, G. A. (2004). Satellite and CALJET Aircraft Observations of Atmospheric Rivers over the Eastern North Pacific Ocean during the Winter of 1997/98. *Monthly Weather Review*, *132*(7), 1721–1745. https://doi.org/10.1175/1520-0493(2004)132<1721:SACAOO>2.0.CO;2

Ralph, F. M., Neiman, P. J., Wick, G. A., Gutman, S. I., Dettinger, M. D., Cayan, D. R., & White, A. B. (2006). Flooding on California's Russian River: Role of atmospheric rivers. *Geophysical Research Letters*, *33*(13). https://doi.org/10.1029/2006GL026689

Ralph, F. M., Ralph, F. M., T. Coleman, T. Coleman, Coleman, T., Neiman, P. J., Neiman, P. J., Zamora, R. J., Dettinger, M. D., & Dettinger, M. D. (2012). Observed

impacts of duration and seasonality of atmospheric-river landfalls on soil moisture and runoff in coastal northern California. *Journal of Hydrometeorology, 14,* 443–459. https://doi.org/10.1175/jhm-d-12-076.1

Ralph, F. M., Rutz, J. J., Cordeira, J. M., Dettinger, M., Anderson, M., Reynolds, D., Schick, L. J., & Smallcomb, C. (2019). A Scale to Characterize the Strength and Impacts of Atmospheric Rivers. *Bulletin of the American Meteorological Society, 100*(2), 269–289. https://doi.org/10.1175/BAMS-D-18-0023.1

Reidmiller, D., Avery, C. W., Avery, C. W., Easterling, D. R., Easterling, D. R., Kunkel, K., Kunkel, K. E., Lewis, K. L. M., Maycock, T. K., B.C. Stewart, & Stewart, B. C. (2017). *Impacts, Risks, and Adaptation in the United States: Fourth National Climate Assessment, Volume II*. https://doi.org/10.7930/nca4.2018

Ryoo, J.-M., Kaspi, Y., Waugh, D. W., Kiladis, G. N., Waliser, D. E., Duane E. Waliser, Fetzer, E. J., & Kim, J. (2013). Impact of Rossby Wave Breaking on U.S. West Coast Winter Precipitation during ENSO Events. *Journal of Climate*, *26*(17), 6360–6382. https://doi.org/10.1175/jcli-d-12-00297.1

Sammon, J. W. (1969). A Nonlinear Mapping for Data Structure Analysis. *IEEE Transactions on Computers*, *C–18*(5), 401–409. https://doi.org/10.1109/T-C.1969.222678

Schlef, K. E., Moradkhani, H., & Lall, U. (2019). Atmospheric Circulation Patterns Associated with Extreme United States Floods Identified via Machine Learning. *Scientific Reports*, *9*(1), Article 1. https://doi.org/10.1038/s41598-019-43496-w

Seneviratne, S.I., Zhang, X., Adnan, M., Badi, W., Dereczynski, C., Di Luca, A., Ghosh, S., Iskandar, I., Kossin, J., Lewis, S., Otto, F., Pinto, I., Satoh, M., Vicente-Serrano, S.M., Wehner, M., & Zhou, B. (2021). Weather and Climate Extreme Events in a Changing Climate. In Masson-Delmotte, V., Zhai, P., Pirani, A., Connors, S.L., Péan, C., Berger, S., Caud, N., Chen, Y., Goldfarb, L., Gomis, M.I., Huang, M., Leitzell, K., Lonnoy, E., Matthews, J.B.R., Maycock, T.K., Waterfield, T., Yelekçi, O., Yu, R., & Zhou, B. (Eds.), *Climate Change 2021: The Physical Science Basis. Contribution of Working Group I to the Sixth Assessment Report of the Intergovernmental Panel on Climate Change* (pp. 1513–1766). Cambridge University Press, Cambridge, United Kingdom and New York, NY, USA. doi: 10.1017/9781009157896.013.

Sheridan, S. C., & Lee, C. C. (2011). The self-organizing map in synoptic climatological research. *Progress in Physical Geography: Earth and Environment*, *35*(1), 109–119. https://doi.org/10.1177/0309133310397582

Slinskey, E. A., Loikith, P. C., Waliser, D. E., Guan, B., & Martin, A. (2020). A Climatology of Atmospheric Rivers and Associated Precipitation for the Seven U.S. National Climate Assessment Regions. *Journal of Hydrometeorology*, *21*(11), 2439–2456. https://doi.org/10.1175/JHM-D-20-0039.1

Smith, B., Yuter, S. E., Neiman, P. J., & Kingsmill, D. E. (2010). Water Vapor Fluxes and Orographic Precipitation over Northern California Associated with a Landfalling Atmospheric River. *Monthly Weather Review*, *138*(1), 74–100. https://doi.org/10.1175/2009mwr2939.1

Waliser, D. E., & Guan, B. (2017). Extreme winds and precipitation during landfall of atmospheric rivers. *Nature Geoscience*, *10*(3), 179–183. https://doi.org/10.1038/ngeo2894

Xia, Y., Mitchell, K., Ek, M., Cosgrove, B., Sheffield, J., Luo, L., Alonge, C., Wei, H., Meng, J., Livneh, B., Duan, Q., & Lohmann, D. (2012). Continental-scale water and energy flux analysis and validation for North American Land Data Assimilation System project phase 2 (NLDAS-2): 2. Validation of model-simulated streamflow. *Journal of Geophysical Research: Atmospheres*, *117*(D3). https://doi.org/10.1029/2011JD016051

Xia, Y., Mitchell, K., Ek, M., Sheffield, J., Cosgrove, B., Wood, E., Luo, L., Alonge, C., Wei, H., Meng, J., Livneh, B., Lettenmaier, D., Koren, V., Duan, Q., Mo, K., Fan, Y., & Mocko, D. (2012). Continental-scale water and energy flux analysis and validation for the North American Land Data Assimilation System project phase 2 (NLDAS-2): 1. Intercomparison and application of model products. *Journal of Geophysical Research: Atmospheres*, *117*(D3). https://doi.org/10.1029/2011JD016048

Zhu, Y., & Newell, R. E. (1998). A Proposed Algorithm for Moisture Fluxes from Atmospheric Rivers. *Monthly Weather Review*, *126*(3), 725–735. https://doi.org/10.1175/1520-0493(1998)126<0725:apafmf>2.0.co;2

Appendix. Supplemental Materials

Measuring moisture and its transport are critical in understanding and predicting storms associated with extreme precipitation events. Integrated Water Vapor (IWV), also known as precipitable water, is a measurement of the amount of water vapor present within an atmospheric column. IWV is useful in identifying regions with high moisture content and the origins of moisture transported to the midlatitudes during ARs. The flux of this moisture, however, is also important in characterizing ARs and evaluating their associated impacts (Lavers et al., 2016; Neiman et al., 2008; Waliser & Guan, 2017).

Integrated Water Vapor Transport (IVT) is a measurement of horizontal moisture flux and is the product of water vapor mass and horizontal wind speeds integrated throughout an atmospheric column. This is calculated as:

$$IVT = -\frac{1}{g}\int_{p_s}^{p_t} q\boldsymbol{V}_h \, dp \, ,$$

where g is the gravitational acceleration constant, q is the specific humidity, and $\boldsymbol{V}_h$ is the horizontal wind vector. Values are integrated across pressure levels from p_s, 1000 hPa, to p_t, 200 hPa. The integration occurs using MERRA-2 data across pressure levels at every 25 hPa from 1000 to 700 and every 50 from 700 to 200 hPa (Gelaro et al., 2017; Ralph et al., 2019). The resulting horizontal moisture flux vectors are largely used to identify, classify, and characterize ARs globally (Guan & Waliser, 2019; Ralph et al., 2019).

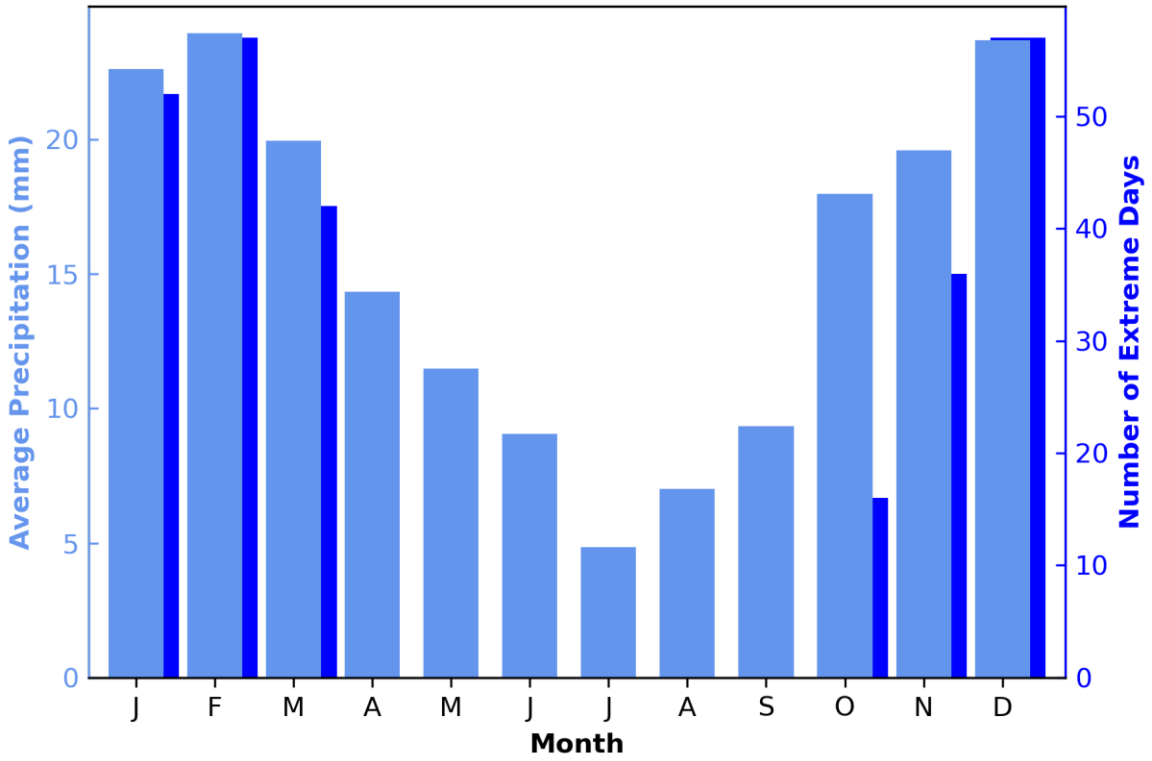

Figure A1. Monthly mean Upper Yuba watershed precipitation (in millimeters) in light blue and the number of extreme (90th percentile) precipitation days in each of the wet season months (October to March) in dark blue, from the 1980 to 2021 climatology.

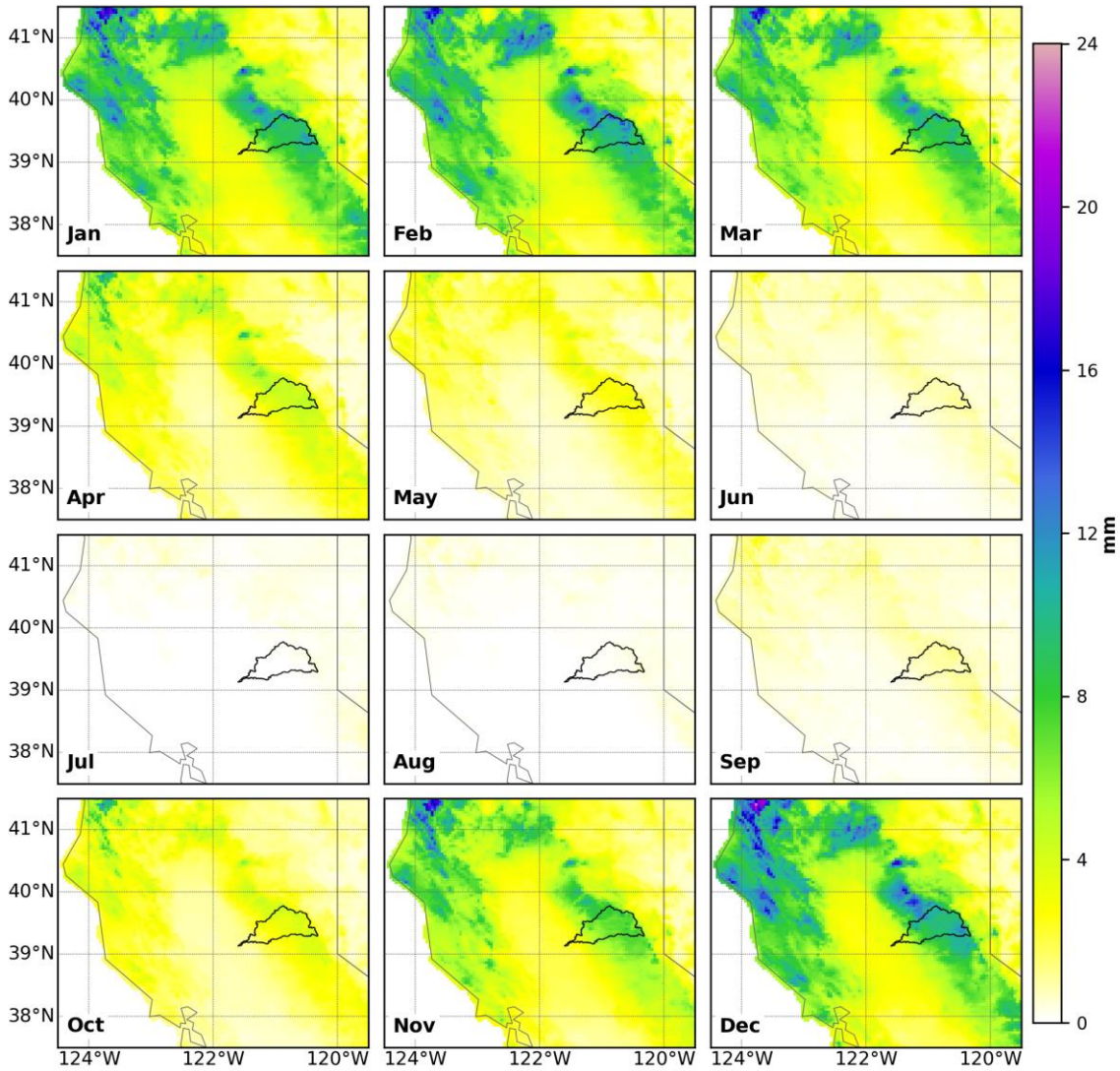

Figure A2. Mean monthly precipitation patterns over the Upper Yuba watershed and surrounding area (in millimeters), from the 1980 to 2021 climatology.

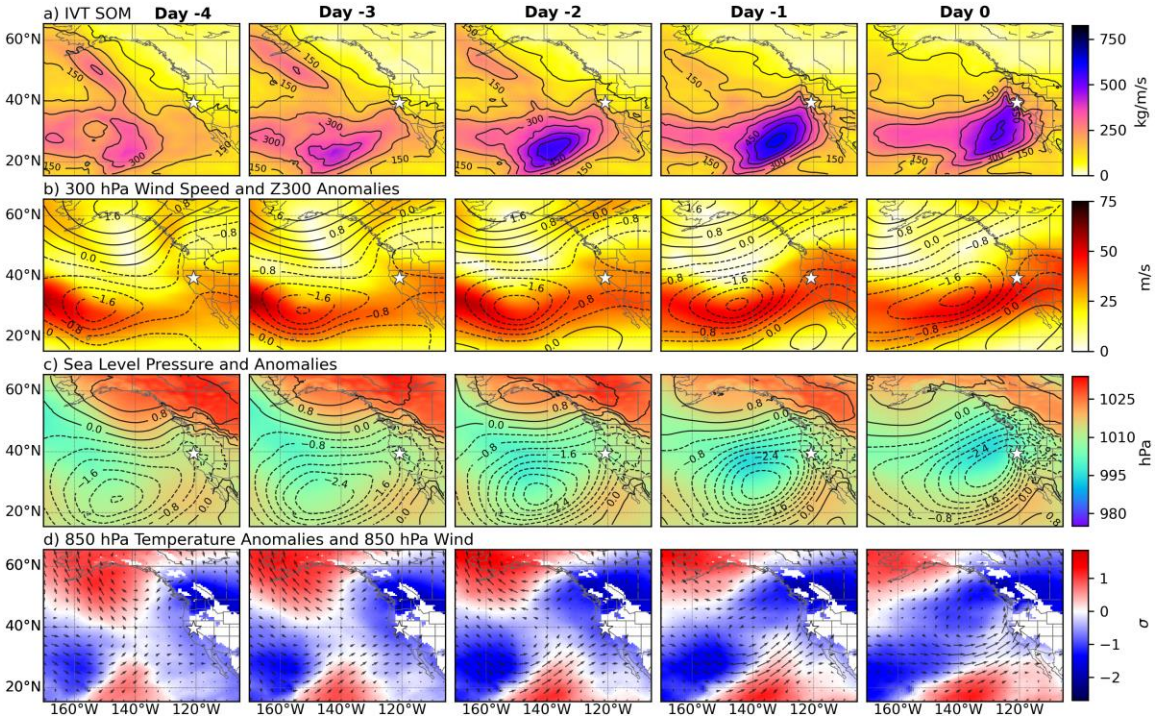

Figure A3. As in Fig. 8 but for Node 2.

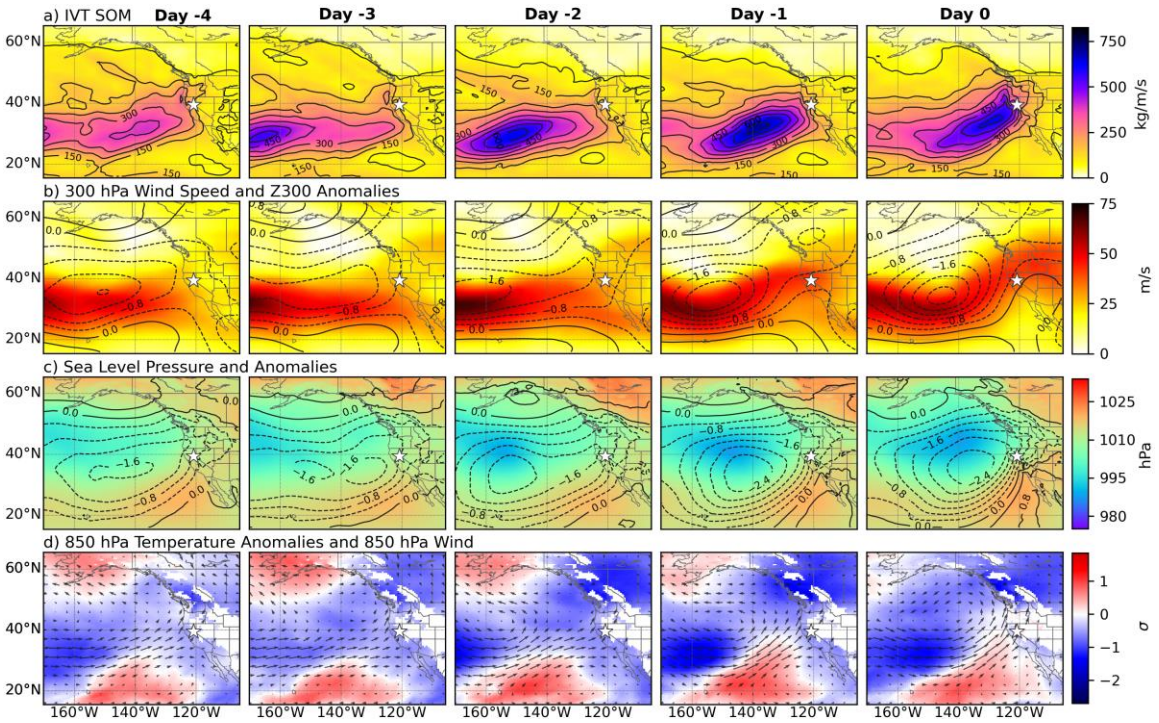

Figure A4. As in Fig. 8 but for Node 4.

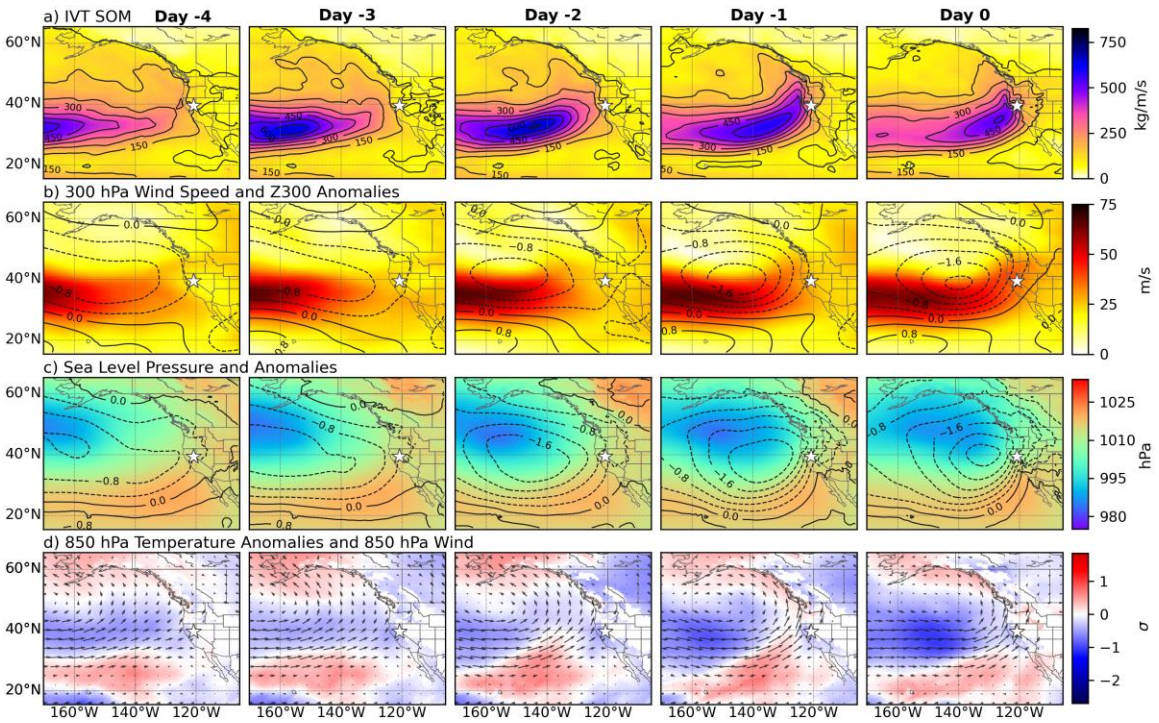

Figure A5. As in Fig. 8 but for Node 7.

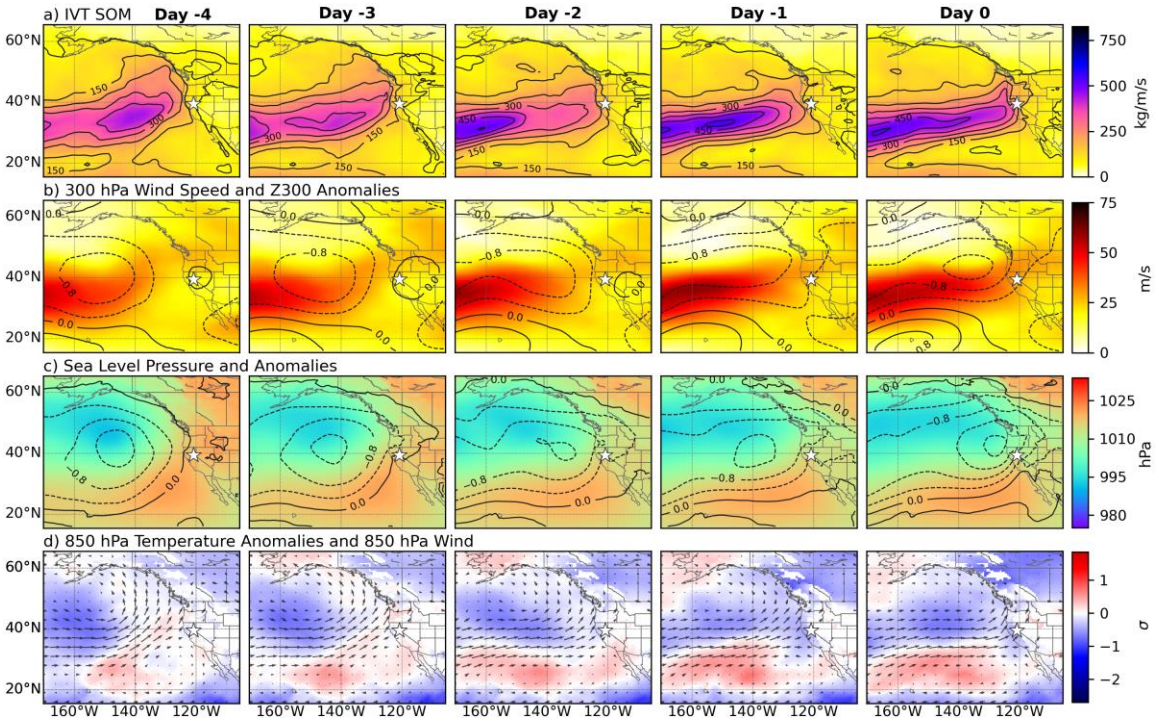

Figure A6. As in Fig. 8 but for Node 8.

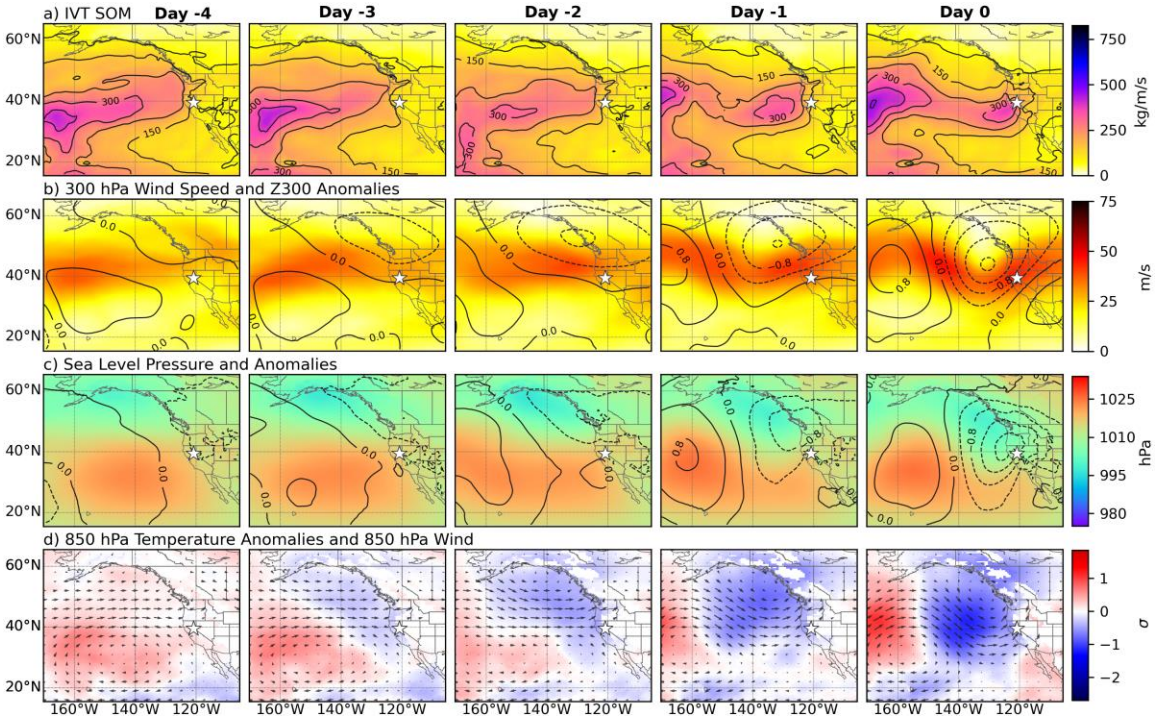

Figure A7. As in Fig. 8 but for Node 9.

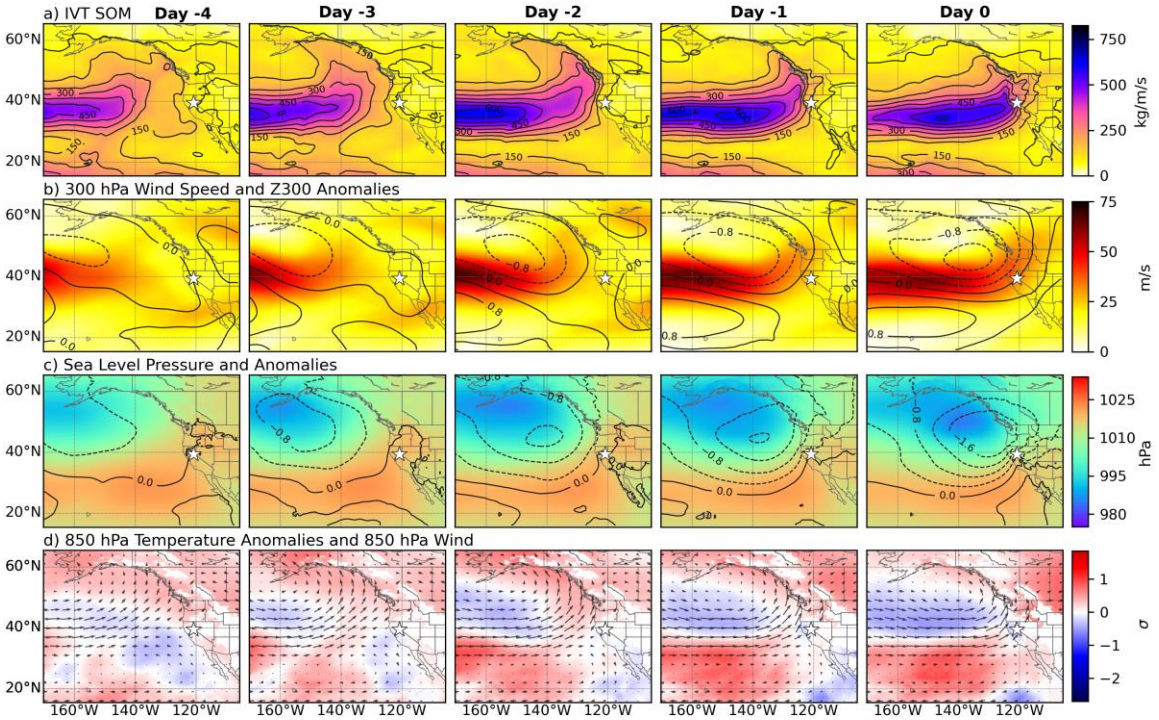

Figure A8. As in Fig. 8 but for Node 11.